

## Accretor stars in massive binaries: testing models on $\zeta$ Ophiuchi

M. RENZO<sup>1,2</sup> AND Y. GÖTBERG<sup>3</sup>

<sup>1</sup>*Department of Physics, Columbia University, New York, NY 10027, USA*

<sup>2</sup>*Center for Computational Astrophysics, Flatiron Institute, New York, NY 10010, USA*

<sup>3</sup>*The Observatories of the Carnegie Institution for Science, 813 Santa Barbara Street, Pasadena, CA 91101, USA*

### ABSTRACT

Most massive stars are born in binary systems close enough for mass-transfer episodes. These modify the appearance, internal structure, and future evolution of both stars. However, models of the accretors are rare. The nearest O-type star to Earth,  $\zeta$  Ophiuchi, has long been proposed to have accreted mass from a former companion, before being ejected as a runaway by the companion’s supernova explosion. Therefore, this star provides an ideal test bed for models of accretors in binaries. We use MESA to model the evolution of a massive binary (initially  $M_1 = 25 M_\odot$ ,  $M_2 = 17 M_\odot$ ) evolving through a stable mass transfer after the donor’s main sequence (case B, initial period 100 days). Adopting common assumptions for the treatment of rotation, chemical mixing, and mass transfer, our accreting star reproduces reasonably well the kinematic, spectroscopic, and photometric properties of  $\zeta$  Ophiuchi. We compare our accretor to fast-rotating single stars: the late spin-up through mass transfer causes the accretor core to spin faster at the end of the main sequence, and the rejuvenation causes an off-center convective layer which impacts the density structure at the envelope base. Our models demonstrate the impact of mass accretion on the secondary star in a binary, with possible implications for its further evolution (either in a binary or as single stars), the final collapse, and the resulting spins of the compact object formed.

*Keywords:* stars: individual:  $\zeta$  Ophiuchi – stars: massive – stars: binaries

### 1. INTRODUCTION

The overwhelming majority of massive stars is born in multiple systems (e.g., Mason et al. 2009; Almeida et al. 2017; Moe & Di Stefano 2017), and a large fraction will exchange mass or merge with a companion in their lifetime (e.g., Sana et al. 2012). The most common type of interaction is a stable mass transfer through Roche Lobe overflow (RLOF) after the end of the donor’s main sequence (case B, Kippenhahn & Weigert 1967), when stars experience most of their radial expansion. Many studies have focused on the dramatic impact these interactions have on the donor star (e.g., Morton 1960; Yoon et al. 2017; Götberg et al. 2017, 2018; Laplace et al. 2020, 2021; Blagorodnova et al. 2021). Often the accreting companion is treated as a point mass. However, binary interactions have a crucial impact on the initially less massive star too.

#### 1.1. *The importance of accretor stars*

During mass transfer, the initially less massive star is expected to accrete mass, spin-up to critical rotation (e.g., Packet 1981), and possibly be polluted by nuclearily processed material from the inner core of the donor star (e.g., Blaauw 1993). The growth of the convective

core due to the increased mass leads to “rejuvenation” of the accretor (e.g., Neo et al. 1977; Schneider et al. 2016). Understanding the evolution of accretors in massive binaries has wide and crucial implications for stellar populations, electromagnetic transient observations, and gravitational-wave progenitors.

Accretors (and merger products) can appear as blue stragglers (e.g., Chen & Han 2009, 2010; Rain et al. 2021) and thus impact cluster populations, their age estimates, and their main sequence (e.g., Pols & Marinus 1994; Wang et al. 2020) and post main sequence morphology (e.g., Wei et al. 2021). The high spin of the accretor post-mass-transfer might be the dominant explanation for the origin of Oe and Be stars (i.e., stars showing emission lines, e.g., Pols et al. 1991; Bodensteiner et al. 2020; Vinciguerra et al. 2020; Dorigo Jones et al. 2020; Wang et al. 2021). Rotationally-mixed accreting stars at low metallicity might also be important for the ionizing flux of high-redshift galaxies (e.g., Eldridge & Stanway 2012).

After mass transfer, the majority of massive binaries will be disrupted by the first supernova, and eject the accretor (“binary SN scenario”, Blaauw 1961; De Donder et al. 1997; Eldridge et al. 2011; Boubert & Evans 2018;

Renzo et al. 2019; Evans et al. 2020). A small fraction of these would be sufficiently fast to become runaway stars, but the majority will be too slow to stand out in astrometric surveys. Assuming a constant star formation history, Renzo et al. (2019) estimated that  $10.1^{+4.6\%}_{-8.6\%}$  ( $0.5^{+2.1\%}_{-0.5\%}$ ) of O-type stars could be slow “walkaway” (runaway) accretors ejected after the companion’s SN explosion. Therefore, presently single O-type stars that accreted mass earlier on contribute to the populations of field massive stars.

From the transients perspective, massive accretor stars are also important: Zapartas et al. (2019) estimated that  $14^{+4\%}_{-11\%}$  of hydrogen (H) rich type II SNe might come from progenitors ejected from a binary after the explosion of their companion. The fact that they accreted mass before exploding can influence their helium (He) core mass and thus the explosion properties and the inferred progenitors (Zapartas et al. 2021). The high post-mass transfer rotation rate of accretor stars in binaries might have implications for the formation of long gamma-ray burst progenitors (e.g., Cantiello et al. 2007).

Finally, the majority of isolated binary evolution scenarios for gravitational-wave progenitors include a common-envelope phase. This is initiated by the originally less massive star, who accretes mass from its companion before the formation of the first compact object (e.g., Belczynski et al. 2016; Tauris et al. 2017; Broekgaarden et al. 2021). Therefore, it is possible that accretion of mass before the formation of the first compact object could modify the internal structure of the star that will initiate the common-envelope (e.g., Law-Smith et al. 2020; Klencki et al. 2021). Specifically, the rotation rate, chemical composition, and innermost structure of the envelope (because of rejuvenation) will differ from a single star.

Despite their importance, accretor stars in binaries have so far received much less attention than the donor stars, with the pioneering studies of Ulrich & Burger (1976); Hellings (1983, 1984), and Braun & Langer (1995) as notable exceptions. Large grids of accretor models are lacking, most of the studies focus on lower mass systems (e.g.,  $M_1 \lesssim 16 M_\odot$  in van Rensbergen et al. 2011) or neglect the crucial impact of rotation (e.g., Sravan et al. 2019, but see also Wang et al. 2020) and only few sparse massive models exist (e.g., Cantiello et al. 2007).

Modeling accretor stars requires following the coupled evolution of two rotating stars exchanging mass. Making robust predictions is challenging because of the admittedly large number of free parameters necessary to model each individual star and their interactions. Rapid

population synthesis typically cannot include the effects of binary mass transfer on the internal structure of the stars, and rely on the implicit assumption that the accretor is sufficiently well described by a (possibly fast-rotating) single star model. Here, we compute detailed evolutionary models of both stars in a binary and compare our accretor to rotating single star models to test this assumption.

## 1.2. A prototypical example of accretor: $\zeta$ Ophiuchi

The nearest O-type star to Earth,  $\zeta$  Ophiuchi ( $\zeta$  Oph) provides a unique opportunity to constrain massive binary evolution models.  $\zeta$  Oph has a distance from Earth of  $107 \pm 4$  pc (Neuhäuser et al. 2020, and references therein), and a spectral type O9.5IVnn (Sota et al. 2014). It occasionally shows emission lines, making it an Oe star (Walker et al. 1979; Vink et al. 2009). Its surface rotation rate is extremely large, with most estimates of the projected rotational velocity from optical spectra exceeding  $v \sin(i) \gtrsim 400$  km s $^{-1}$  (corresponding to the “nn” in the spectral type, Zehe et al. 2018 and references therein). By comparing the observed  $v \sin(i) = 432 \pm 16$  km s $^{-1}$  to the theoretical breakup rotation, Zehe et al. (2018) constrained the inclination angle to  $i \gtrsim 56$  degrees. Using optical interferometry, Gordon et al. (2018) measured the centrifugal distortion of  $\zeta$  Oph, finding a polar radius of  $7.5 R_\odot$  and centrifugally increased equatorial radius of  $9.1 R_\odot$ , corresponding to a  $v \sin(i) = 348$  km s $^{-1}$ .

$\zeta$  Oph was originally identified as a runaway because of its large proper motion by Blaauw (1952). Unfortunately, the *Gaia* data for this object are not of sufficient quality<sup>1</sup> to improve previous astrometric results, but estimates of the peculiar velocity range in  $30 - 50$  km s $^{-1}$  (e.g., Zehe et al. 2018; Neuhäuser et al. 2020). The large velocity with respect the surrounding interstellar material is also confirmed by the presence of a prominent bow-shock (e.g., Bodensteiner et al. 2018).

Because of its young apparent age, extremely fast rotation, and nitrogen (N) and He rich surface (e.g., Herrero et al. 1992; Blaauw 1993; Villamariz & Herrero 2005; Marcolino et al. 2009),  $\zeta$  Oph is a prime example of runaway from the binary SN scenario (Blaauw 1993). Many studies have suggested  $\zeta$  Oph might have accreted mass from a companion before acquiring its large velocity, both from spectroscopic and kinematic considerations (e.g., Blaauw 1993; Hoogerwerf et al. 2000, 2001; Tetzlaff et al. 2010; Neuhäuser et al. 2020) and using stellar modeling arguments (e.g., van Rensbergen et al.

<sup>1</sup> The renormalized unit weighted error (RUWE) of this star in Gaia EDR3 is 4.48.

1996). Recently, Neuhäuser et al. (2020) suggested that  $1.78 \pm 0.21$  Myr ago a SN in Upper-Centaurus-Lupus produced the pulsar PSR B1706-16, ejected  $\zeta$  Oph, and also injected the short-lived radioactive isotope  $^{60}\text{Fe}$  on Earth. This argues strongly for a successful SN explosion of the companion with a  $\sim 250 \text{ km s}^{-1}$  natal kick, sufficient in most cases to disrupt the binary (e.g., Tauris 2015; Renzo et al. 2019; Evans et al. 2020).

Although the nature of  $\zeta$  Oph as a binary product is well established, because of its observed large surface rotation rate, previous attempts to model it rely purely on rotational mixing to explain the N- and He-rich surface composition (e.g., Maeder & Meynet 2000). Even the binary models of van Rensbergen et al. (1996) assumed rotational mixing from the inside of the accreting star driven by the spin-up during mass transfer (see also Cantiello et al. 2007). However, Villamariz & Herrero (2005) (hereafter, VH05) were unable to obtain a satisfying fit for the stellar spectra using the single-star rotating models from Meynet & Maeder (2000, 2003): by the time rotational mixing enriches the surface, single massive stars have significantly spin down through wind mass loss.

This may not be surprising: parametrized models of rotational mixing predict lower efficiency for metal-rich and relatively low mass stars. The reason is the increased importance of mean molecular weight gradients and the longer thermal timescales compared to more massive stars (e.g., Yoon et al. 2006; Perna et al. 2014). The parent association of  $\zeta$  Oph has a metallicity  $Z = 0.01 \simeq Z_\odot$  (based on asteroseismology from Murphy et al. 2021), and mass estimates for  $\zeta$  Oph range from  $13 - 25 M_\odot$ , at the lower end of the range where rotational mixing can efficiently bring He and CNO-processed material to the surface (chemically homogeneous evolution, Maeder & Meynet 2000).

Given the challenges in explaining the surface composition of  $\zeta$  Oph as a rotating single star and the evidence for its past as a member of a binary system, this star offers a unique opportunity to constrain the evolution of accretors in massive binaries. Here, we present self-consistent binary evolution models for  $\zeta$  Oph computing simultaneously the coupled evolution of *both* donor and accretor star and their orbit. After describing our MESA setup in Sec. 2, we present a model which reproduces the majority of the salient features of this star in Sec. 3. We discuss the sensitivity of our results to the admittedly many free parameters in Sec. 4, before concluding in Sec. 5.

## 2. MODELING MASSIVE BINARIES WITH MESA

Modeling the evolution of massive binaries ( $M_1 \gtrsim 20 M_\odot \geq M_2$ ) is challenging because of the intricate role of several notoriously difficult stellar physics ingredients (accretion, differential rotation, mixing, high mass-loss rates, etc.). We follow self-consistently the coupled evolution of two massive stars in a binary system using MESA (version 15140, Paxton et al. 2011, 2013, 2015, 2018, 2019). Our choice of input parameters and our numerical results are available at <https://doi.org/10.5281/zenodo.4701565>. We discuss here only the main relevant physical parameters and describe tests changing some of the fiducial values in Sec. 4. Appendix A gives more details on our choice of input physics, and appendix B discuss the numerical resolution in space and time.

We adopt the Ledoux (1947) criterion to determine convective stability and a mixing length parameter of 1.5. We allow for time-dependent convection as in Renzo et al. (2020) based on Arnett (1969). We include semiconvection and thermohaline mixing following Langer et al. (1983) and Kippenhahn et al. (1980), respectively, each with efficiency 1.0. We use the exponential core overshooting from Herwig (2000) with free parameters  $(f, f_0) = (4.25 \times 10^{-2}, 10^{-3})$  (Claret & Torres 2017) which broadly reproduce the width of the main sequence from Brott et al. (2011). We do not use over/undershooting for off-center convective shells. We also use the local implicit enhancement of the convective flux in superadiabatic regions introduced in MESA 15140.

We treat rotation in the “shellular” approximation (e.g., Zahn 1992; Ekström et al. 2012), that is we assume constant rotational frequency  $\omega$  along isobaric surfaces. Furthermore, we assume tidal synchronization and rigid rotation at zero age main sequence (ZAMS) – the beginning of our runs. For our fiducial period of  $P = 100$  days, this means the stars are initially slow rotators: the surface averaged rotational velocity is  $\lesssim 3 \text{ km s}^{-1}$  for both. Our models include a diffusive approximation for meridional currents (Eddington-Sweet circulations, Sweet 1950), which dominate the chemical mixing due to rotation. We also include the secular and dynamical shear instabilities, and the Goldreich-Schubert-Fricke (GSF) instability. We assume a Spruit-Taylor dynamo for the transport of angular momentum (Spruit 2002), and chose the same free parameters as Heger et al. (2000). This also includes the implicit rotational enhancement of wind mass loss to keep the rotation sub-critical as in Langer (1998). Specifically, at each timestep we calculate a wind enhancement factor to reduce the ratio  $\omega/\omega_{\text{crit}} \lesssim 0.95$  where  $\omega_{\text{crit}} = \sqrt{(1 - L/L_{\text{Edd}})GM/R^3}$  and  $L_{\text{Edd}}$  is the Eddington luminosity computed using the stellar opacity down to optical depth  $\tau = 2/3$ ,  $L$  is the luminosity,  $R$  the

(equatorial) radius, and  $G$  the gravitational constant. However, we allow a tolerance of 0.05 on this limit.

We assume a fiducial metallicity of  $Z = 0.01$  informed by the present-day  $Z$  of  $\zeta$  Oph's parent cluster (Murphy et al. 2021), and assume the relative element abundances to scale with solar values (Grevesse & Sauval 1998). We include wind mass loss following Vink et al. (2000, 2001) for effective temperature  $T_{\text{eff}} \gtrsim 10^{4.2}$  K, and de Jager et al. (1988) for  $T_{\text{eff}} \lesssim 10^{4.2}$  K, both with a scaling factor of 1. Nominally, this means our wind mass-loss rate post-mass transfer is overestimated by about a factor of 100 compared to observations (weak wind problem, see Marcolino et al. 2009). However, Lucy (2012) and Lagae et al. (2021) proposed that the temperature structure of the winds of low-luminosity O-type stars might affect the spectral lines and cause an empirical underestimate of the mass-loss rate. After the end of mass transfer, we use the Nugis & Lamers (2000) wind mass loss rate for the hot and H-deficient donor star.

Both stars are evolved simultaneously on the same timesteps until after the donor detaches from its Roche lobe. We follow Kolb & Ritter (1990) to calculate with an implicit scheme the mass transfer rate. Moreover, we assume that the specific angular momentum and entropy of the transferred layers match the surface of the accretor, while the chemical composition is set by the stratification of the donor star. Mass transfer is conservative until the accretor reaches critical rotation, after which rotationally-enhanced mass loss governs the mass transfer efficiency. Transferred matter which is not successfully accreted carries away the specific angular momentum corresponding to the accretor's orbital motion.

After losing their envelopes, massive donors are not expected to expand to hundreds of  $R_{\odot}$  during He-shell burning at the metallicity we consider (e.g., Laplace et al. 2020, however see also Gilkis et al. 2019). Thus, we stop evolving a binary system when the donor's surface He mass fraction is larger than 0.35 – indicating that a significant amount of envelope has been lost or transferred, and the radius is smaller than both the Roche radius and the ZAMS radius. From here onwards, we continue the evolution of the accretor as a single star until its terminal-age main sequence (TAMS, defined as when the central mass fraction of H drops below  $10^{-4}$ ) with the same setup.

### 3. MASSIVE BINARY EVOLUTION NATURALLY EXPLAINS $\zeta$ OPHIUCHI'S PROPERTIES

We describe here the evolution of a binary system where the accretor star can broadly reproduces all the observed features of  $\zeta$  Oph. We assume initial masses  $M_1 = 25 M_{\odot}$ ,  $M_2 = 17 M_{\odot}$ , and initial period  $P =$

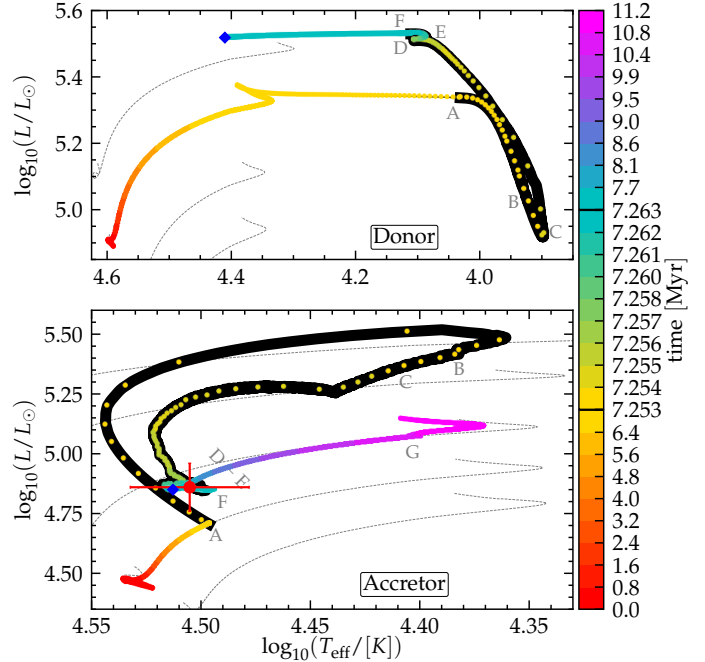


**Figure 1.** HR diagram for the donor star (top) and accretor star (bottom) of the progenitor binary of  $\zeta$  Oph. Each point is separated by 50 years, and the black outline corresponds to the RLOF phase. The colors show the age on a non-uniform scale: we use smaller time-bins during RLOF ( $7.25 \text{ Myr} \lesssim t \lesssim 7.26 \text{ Myr}$ ). The red data point shows the position of  $\zeta$  Oph according to VH05, and the blue diamonds mark the end of the binary run. We continue the accretor evolution as a single star from there until core H depletion, hence the bottom panel shows a longer time. We emphasize the different scales on the two panels. The thin gray dashed line show the main sequence evolution of non-rotating single stars of  $15$ ,  $17$ ,  $20$ ,  $25$ , and  $30 M_{\odot}$  at  $Z = 0.01$  for comparison.

100 days (corresponding to a separation  $a \simeq 314 R_{\odot}$ ) with a metallicity of  $Z = 0.01$ .

Fig. 1 shows the Hertzsprung-Russell (HR) diagrams of both stars, the donor and accretor are shown separately on the top and bottom panel, respectively (see Fig. 8 for an HR diagram of both stars on the same scale). After  $\sim 7.24$  Myr, the donor star evolves off the main sequence and  $\sim 8400$  years later, at point A in Fig. 1, it overfills its Roche lobe. This results in a stable case B RLOF on a thermal timescale from point A to F (black outline of the curves). We refer to Götberg et al. (2017); Klencki et al. (2020); Laplace et al. (2021); Blagorodnova et al. (2021) and references therein for a detailed description of the evolution of massive donor stars in binaries. Although our models are more massive, the qualitative behavior of the donor star is similar. Minor differences might arise because of mixing above and in the H-burning shell (e.g., Schootemeijer et al.

2019; Klenki et al. 2021), and its interplay with the mass transfer.

At the onset of RLOF (point A in Fig. 1), the accretor star is still on the main sequence with  $T_{\text{eff}} \simeq 10^{4.5}$  K and its central mass fraction of hydrogen is  $X(^1\text{H}) \simeq 0.42$ . Because of accretion, it is pushed out of thermal equilibrium and quickly becomes over-luminous to radiate away the excess internal energy. The accretor reaches  $L \simeq 10^{5.5} L_{\odot} \gg L_{\text{nuc}} \simeq 10^{5.1} L_{\odot}$ , with  $L_{\text{nuc}}$  the total energy released per unit time by nuclear burning (integrated throughout the star).

The radius of the accretor increases dramatically from  $\sim 7.5 R_{\odot}$  to  $\sim 35 R_{\odot}$ , and only once the accretor reaches critical rotation (roughly at point B in the bottom panel of Fig. 1, roughly at the lowest  $T_{\text{eff}}$ ), the star begins contracting and its  $T_{\text{eff}}$  increases. At  $T_{\text{eff}} \simeq 10^{4.43}$  K, slightly after point C, the material transferred from the donor star becomes progressively more He-rich and CNO-processed, changing the opacity in the outer-layers of the accretor and causing a kink in its evolutionary track. This indicates that the partially processed outer layers<sup>2</sup> of the donor’s core are uncovered by mass transfer. Thus, late during the mass transfer, material with a high mean molecular weight  $\mu$  is placed on top of the comparatively low- $\mu$  primordial envelope of the accretor, modifying the morphology of the evolutionary track.

Because of the inverted  $\mu$ -gradient, thermohaline mixing starts in the outer layers of the accreting star, and, together with rotational mixing, it progressively dilutes the surface  $^4\text{He}$  and  $^{14}\text{N}$  mass fractions and causes noisy features from point D to F on the HR diagram of the accretor (e.g., Cantiello et al. 2007). From D to E the donor star briefly expands again: by point D the surface is He-rich, and partial recombination of  $^4\text{He}$  drives a convective layer which is extremely thin in mass ( $\lesssim 10^{-4} M_{\odot}$ ) but can expand to significantly large radii<sup>3</sup>.

We emphasize that our adopted (standard) choices to model mixing and rotation are likely to impact the morphology of the accretor’s evolutionary track during RLOF. The entire duration of RLOF from A to F is only about  $10^4$  years - of the order of the thermal timescale of the donor star. Moreover, the accretor spends most of this time close to the final, post-RLOF position (blue diamond in the bottom panel). Therefore, observation of a (population of) mass-transferring binary(ies) is un-

likely to provide a direct probe of the accuracy of our mixing treatment. We expand on the mixing processes inside the accretor in Sec. 3.1.

We evolve the binary system until the blue diamonds in Fig. 1, which occurs well after the donor detaches from the Roche Lobe. At this point, the accretor is a H-rich fast-rotating star of  $\sim 20.1 M_{\odot}$ . Available mass estimates for the presently single  $\zeta$  Oph are highly uncertain but they typically include  $20 M_{\odot}$  in their range (e.g., Hoogerwerf et al. 2001, VH05, Neuhauser et al. 2020). The accretor’s post-RLOF orbital velocity is  $v_2 \simeq 52 \text{ km s}^{-1}$ . In the subsequent evolution, wind mass loss from both stars will widen the binary and decrease the orbital velocity of the accretor. We computed one binary until the end of the donor’s He core burning, and at that point the accretor’s orbital velocity has decreased to  $\sim 40 \text{ km s}^{-1}$ . Further decrease during the remaining evolution is expected because of wind mass loss from both stars, likely dominated by the (uncertain) mass-loss rate of the stripped donor star. Nevertheless, the value we obtain is in broad agreement with estimates of the observed runaway velocity of  $\zeta$  Oph.

Accounting for both wind mass loss and the amount of mass transferred, at the end of RLOF the donor becomes a He star of  $\sim 9.4 M_{\odot}$ , likely to contract further. Depending on its wind mass-loss rate, the stripped donor’s spectrum might show absorption lines, emission lines, or a mixture of both (e.g., Crowther 2007; Neugent et al. 2017; Götberg et al. 2018). Its surface H mass fraction is  $\lesssim 0.2$  and even this residual H-rich layer might possibly be removed by further wind mass loss (e.g., Yoon et al. 2017; Götberg et al. 2017).

After the donor detaches from its Roche lobe and contracts to a radius smaller than at TAMS (blue diamonds in Fig. 1), we continue the evolution of the accretor as a single star with the same MESA setup until its TAMS. The main-sequence track on which the accretor settles post-RLOF has a higher luminosity compared to the original track because of the accretion of mass, and its slope is slightly steeper due to the close-to-critical rotation and the accretion of partially nuclearly processed (He- and N-rich) material.

Errorbars in the bottom panel of Fig. 1 mark the approximate position of  $\zeta$  Oph based on the spectral analysis of VH05. The colors of the track in Fig. 1 indicate that our accreting star spends about  $\sim 2$  Myr within the represented errorbars after the end of RLOF. Assuming the kinematic age of  $1.78 \pm 0.21$  (Neuhäuser et al. 2020), together with the remaining lifetime of the donor of  $\sim 0.5$  Myr, our model approximately produces the correct timescale for the binary SN scenario. Moreover, according to our model, the present-day age

<sup>2</sup> These are left behind by the recession in mass coordinate of the core during the donor’s main sequence.

<sup>3</sup> With previous MESA releases, we found it challenging to compute models beyond this phase: the large increase in radius impacts significantly the mass transfer rate.

of  $\zeta$  Oph is  $\sim 9.5$  Myr. The age of the parent association Upper-Centaurus-Lupus is relatively uncertain, with estimates from pre-main sequence isochrone fitting of about  $9 \pm 1$  Myr, but an average age of  $15 \pm 3$  Myr (Pecaut & Mamajek 2016). However, given the sensitivity of our model to rejuvenation (see Sec. 3.1.1), the large age scatter of the region, and the unknown systematics in age measurements, we consider our model broadly compatible with the existing constraints.

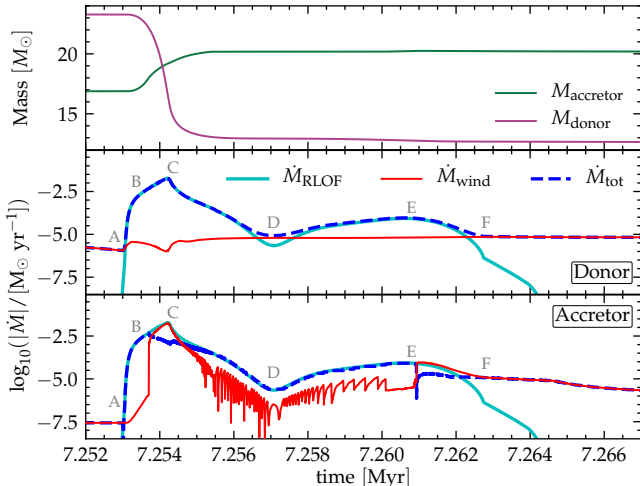


**Figure 2.** The top panel shows the total mass of each star as a function of time during RLOF. The middle and bottom panel show the contributions to the rate of mass change for the donor and accretor star, respectively. The cyan solid lines show the mass transfer rate due to RLOF, the red lines show the (mechanically enhanced) wind mass loss rates, and dashed blue lines show their combination giving the actual rate of mass change. During RLOF the accretor reaches critical rotation, which leads to oscillations in the rotationally-enhanced wind mass loss.

Fig. 2 shows the mass evolution (top panel) and the rate of mass change (middle and bottom panel) for each star during RLOF. The middle panel focuses on the donor star which loses mass via RLOF (cyan line) and winds (thin red line). The dashed blue lines show their combination resulting in the actual rate of mass change of the stars. The bottom panel shows instead the accreting star, which grows in mass because of the mass transfer. At peak (point C), the mass transfer rates reaches values above  $10^{-2} M_{\odot} \text{ yr}^{-1}$  and taps into the optically thick matter of the donor (i.e., the donor’s Roche radius becomes smaller than its photosphere  $R_{\text{RL},1} < R_1$ ).

Initially, between point A and B, the mass transfer rate equals the mass accretion rate (bottom panel of Fig. 2), that is initially the accretion is (by construction) fully conservative. The bulk of the mass is accreted during this initial phase which lasts about  $\sim 2 \times 10^3$  years.

As the mass and surface rotation rate of the accretor increase, the assumed rotational-enhancement of the wind progressively increases the mass-loss rate by  $\sim 5$  orders of magnitude. The mechanically-enhanced wind controls the accretion efficiency, and at  $\sim 7.254$  Myr (from B to C, where the red solid line and the cyan line overlap) the mass transfer becomes briefly non-conservative: the majority of the mass transferred during this phase is ejected, we assume as a fast wind from the vicinity of the accretor. Consequently, the accretor slightly spins down and starts contracting (cf. Fig. 1). In the remaining evolution from C to F, the interplay between the wind mass loss rate, the spin-up due to accretion and the spin-down due to inward transport of angular momentum (see Sec. 3.2) trigger oscillations in the wind mass loss rate. Nevertheless, for most of the evolution, accretion, albeit not-fully conservative, still occurs. This allows for CNO-processed material from the donor to reach the surface of the accretor during late stages of mass transfer.

The minimum of the mass transfer rate in point D corresponds to a brief phase of contraction (see also Fig. 1). However, from D-E, the donor star briefly expands again ( $T_{\text{eff}} \simeq 10^{4.1} \text{ K}$ ,  $L \simeq 10^{5.5} L_{\odot}$ ). This is due to the partial recombination of the now He-rich outer layers, which causes a transient surface convection layer. This causes a radial expansion of the outer convective layers and an increase in the mass-transfer rate, despite at this point the donor is less massive than the accretor and the binary is widening. During this phase, the mass transfer becomes highly non-conservative again (in the bottom panel the wind and the mass accretion rate nearly cancel each other again at  $\sim 7.261$  Myr), until the donor completely detaches from its Roche lobe at point F.

### 3.1. Mixing and composition

MESA treats mixing in diffusion approximation (Paxton et al. 2011). To illustrate the dominant processes throughout the accretor’s evolution, we show in Fig. 3 the diffusion coefficients for various mixing processes as a function of mass coordinate at selected times. Specifically, we show from top to bottom:

- main sequence before RLOF (i.e., before point A in Fig. 1 and Fig. 2);
- beginning of RLOF (between point A and B);
- late during RLOF (between point C and D);
- predicted present-day structure of  $\zeta$  Oph (post-RLOF within the red error-bar on Fig. 1);
- close to TAMS (point G in Fig. 1).

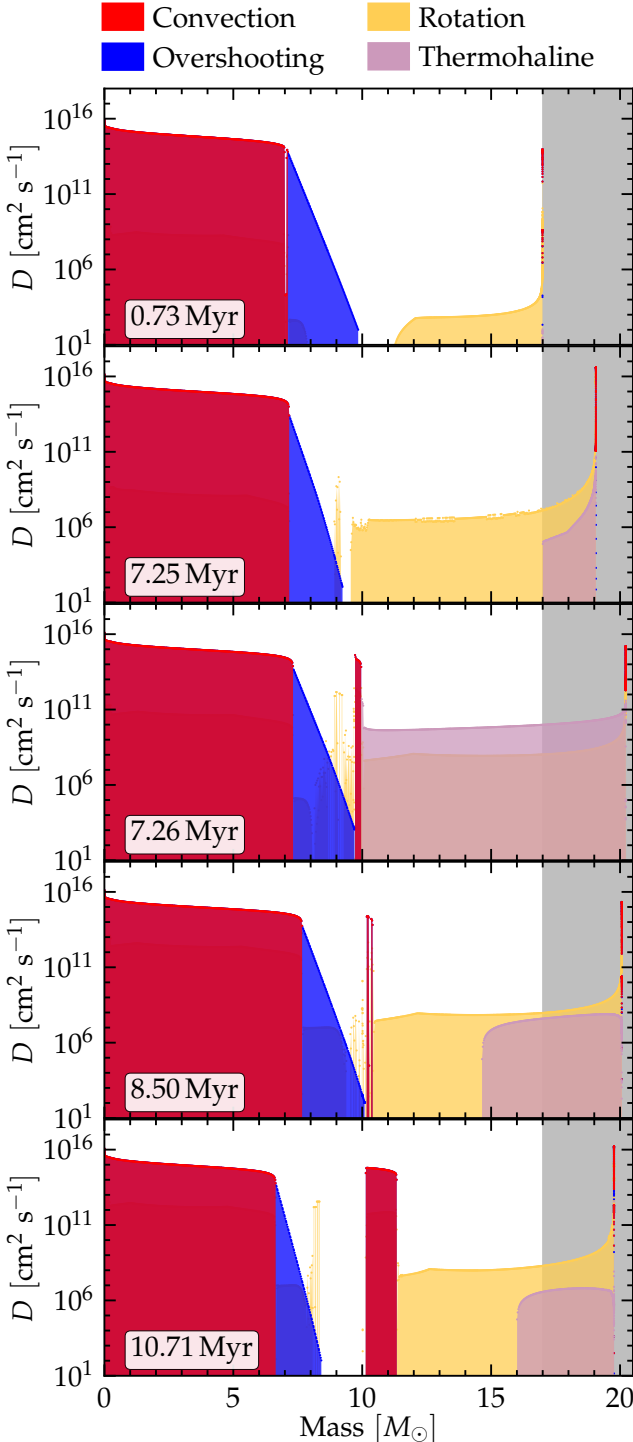


**Figure 3.** Mixing diffusion coefficients in the accretor star. The gray area on the right highlights accreted material. From top to bottom, each panel shows a profile during the main sequence (before point A in Fig. 1), early during RLOF (close to point C), mid-RLOF (close to point D), late during RLOF (between point D and E), and after RLOF (point G). A movie of the entire evolution is available at <https://doi.org/10.5281/zenodo.4701565>.

In each panel, the gray background highlights masses larger than the ZAMS mass, which the star can only reach by accreting during RLOF. The colors in Fig. 3 show convection (red), overshooting (blue), rotational mixing (yellow), and thermohaline mixing (pink). Rotational mixing includes all the rotational instabilities that we consider – meridional currents, secular and dynamical shear instabilities, and GSF instability, but throughout the evolution it is strongly dominated by Eddington-Sweet meridional circulations. The only exception is at the interface between core-envelope (i.e., at the outer edge of the overshooting region), where the post-RLOF contraction and spin-up of the core (see Sec. 3.2) can lead to significant dynamical shear (and GSF mixing to a lesser extent). For clarity, we do not show semi-convection which anyways is never the dominant mixing process in our model.

The top panel shows the typical structure of a main sequence massive star: the convective core initially reaching  $\sim 7 M_\odot$  with the overshooting extension to  $\sim 9 M_\odot$ . The slow rotation imparted by the assumed initial tidal synchronization causes a meridional circulation in the envelope (we discuss further the internal rotational structure in Sec. 3.2). Meridional circulations are also present in the core throughout the evolution, but with a diffusivity more than nine orders of magnitude lower than core convection. A small sub-surface convective zone is also appreciable at the very surface (see, e.g., Cantiello et al. 2021).

In the second panel from the top, the star has already accreted  $\sim 2 M_\odot$  (extending in the gray region), and its surface is already spun up to  $\sim 330 \text{ km s}^{-1}$ . Thermohaline mixing has started in the newly accreted layers, but it is subdominant compared to rotational mixing due to meridional circulations in the envelope. Angular momentum transport (by the Spruit-Tayler dynamo) has already imparted some rotation to the inner layers of the envelope. This leads to the disconnected spike in rotational mixing at the outer edge of the core, dominated by dynamical shears. We note that between the top panel and the onset of RLOF, the convective core recedes in mass coordinate, but, by the time shown in the second panel, the accretion of mass has caused the core to grow back to its initial size.

In the third panel, the star has already accreted all the mass that it will, including CNO-enriched layers from the donor’s interior. Thermohaline mixing takes over the dominant role in the envelope (although meridional circulations persist behind it). The increase in core-mass causing the rejuvenation effect is still going on, and the mixing at the core-envelope boundary is partially still due to dynamical shear, but an off center convective re-

gion also appears. Because we adopt an exponentially decreasing overshooting, the diffusion coefficient at the outer edge of the overshooting region is small, and the mixing between the core and the off-center convective region is weak. We do not include over/undershooting for off-center convective layers, which could increase the coupling between these layers. By the fourth panel, roughly corresponding to  $\zeta$  Oph's structure today, thermohaline mixing is progressively shutting down, but some residual mixing at the core edge still remains.

Finally, the last panel shows that as the post-RLOF evolution proceeds, the convection at the outer-edge of the core advances further and remains as a long-lived  $\sim 1 M_\odot$  wide region above the core, but disconnected from it. This is a consequence of core growth because of accretion, and can affect the density profile at the base of the envelope (see also Fig. 7 for its effect on the density profile).

The core growth caused by the accretion of mass, the consequent ingestion in the burning region of fresh H-rich material, and the resulting rejuvenation of the accretor are strongly dependent on the presence of convective boundary mixing. In our model, this is initially provided by overshooting and to a lesser extent dynamical shear (between the top and second panel), at later times, the development of a convective layer above the overshooting region dominates this mixing.

Instead, in the envelope, Eddington-Sweet circulations first dominate, then thermohaline mixing takes over – roughly from the kink after point C in Fig. 1, corresponding to the accretion of CNO-processed material, until the end of RLOF. The combination of these two processes mixes inward material CNO-processed in the donor star and accreted from the surface, and outward CNO-processed material from the core of the accretor.

Tab. 1 summarizes the surface properties of the accretor star at 8.5 Myr (fourth panel of Fig. 3), roughly corresponding to  $\zeta$  Oph's position on the HR diagram today. Both the mass and radius agree reasonably well with the estimates from VH05 and previous studies, that is  $20 M_\odot$  and  $8.3 \pm 1.5 R_\odot$ , respectively. Our radius of  $9.8 R_\odot$  is larger by  $\sim 0.6 R_\odot$  than the equatorial radius recently measured by Gordon et al. (2018), and our model has a  $T_{\text{eff}} \simeq 31\,300$  K, on the lower end of the range considered by VH05. On the other hand, the age of 8.5 Myr is maybe slightly lower than  $\zeta$  Oph's kinematic age plus the entire donor's lifetime. The surface rotational velocity in excess of  $350 \text{ km s}^{-1}$  is also in the correct ballpark albeit possibly on the low end.

We report the surface H mass fraction<sup>4</sup>, lower than primordial because of the accretion of nuclearly processed material, and the surface mass fraction of the most prominent species  $^4\text{He}$ ,  $^{12}\text{C}$ ,  $^{14}\text{N}$ ,  $^{16}\text{O}$ . Assuming our surface H mass fraction  $X(^1\text{H})$ , the corresponding mass fractions of  $^4\text{He}$ ,  $^{12}\text{C}$ ,  $^{14}\text{N}$ ,  $^{16}\text{O}$  obtained by VH05 are  $0.34^{+0.14}_{-0.05}$ ,  $0.0006 \pm 0.0004$ ,  $0.002 \pm 0.001$ , and  $0.005 \pm 0.004$ .

By the accretor's TAMS, rotational mixing (in the form of Eddington-Sweet circulations) and thermohaline mixing nearly homogenize the composition of the envelope of our accretor's model. The surface mass fractions we obtain are sensitive to the interplay between several poorly understood processes treated in one dimension: mass accretion efficiency, rotationally enhanced wind mass loss, thermohaline, and inward rotational mixing. These also impact the composition of the envelope, and thus its radius and  $T_{\text{eff}}$ . Therefore, although not perfect, we consider the match with the mass fractions reported by VH05 surprisingly satisfactory.

### 3.1.1. Comparison to single fast-rotating stars

We now compare the mixing processes in our accretor and in single rotating massive star models. The first four panels of Fig. 4 show the mass fraction of  $^{14}\text{N}$  as a function of mass coordinate along the evolution of four  $20 M_\odot$  stars initialized with  $\omega/\omega_{\text{crit}} = 0.2, 0.3, 0.4, 0.5$ . Except for the initial rotation rate and being single, these stars have the same MESA setup as our binary model. The last panel of Fig. 4 shows our accretor model.

The accretor starts as a  $17 M_\odot$  and is rejuvenated by binary interactions, reaching TAMS at 11.2 Myr. For comparison, the lifetime of a non-rotating single star of  $17 M_\odot$  is  $\sim 11.1$  Myr, while the initially  $20 M_\odot$  rotating models have a main-sequence lifetime of  $\sim 9.2$ - $9.6$  Myr (longer for higher initial rotation rates), hence their TAMS profile are a shade of purple rather than pink in Fig. 4.

The first four panels of Fig. 4 show the typical rotational mixing profiles:  $^{14}\text{N}$  rapidly rises in the core because of the CNO burning, and it is then mixed outwards (as indicated by the arrows in the top left corner of each panel). At any time the  $^{14}\text{N}$  profile is monotonically decreasing in mass coordinate, and the higher the initial rotation, the higher the surface  $^{14}\text{N}$  mass fraction reached at TAMS.

<sup>4</sup> We obtain the mass fractions of individual elements inverting the definition  $\varepsilon(X) = 12 + \log_{10}(N_X/N_H)$ , where  $N_X$  and  $N_H$  are the number fractions of species  $X$  and H, respectively (e.g., Lodders 2019).

$M [M_\odot]$	$R [R_\odot]$	$\omega [\text{days}^{-1}]$	$v_{\text{rot}} [\text{km s}^{-1}]$	$X(^1\text{H})$	$X(^4\text{He})$	$X(^{12}\text{C})$	$X(^{14}\text{N})$	$X(^{16}\text{O})$
20.1	9.8	4.575	361.4	0.678044	0.312058	0.001339	0.001346	0.004149

**Table 1.** Surface properties of the accretor close to the present-day position of  $\zeta$  Oph on the HR diagram, corresponding to a physical age of 8.50 Myr, shortly after the end of RLOF (between the blue diamond and the lower estimate of  $\zeta$  Oph’s  $T_{\text{eff}}$  in Fig. 1, third panel of Fig. 3).

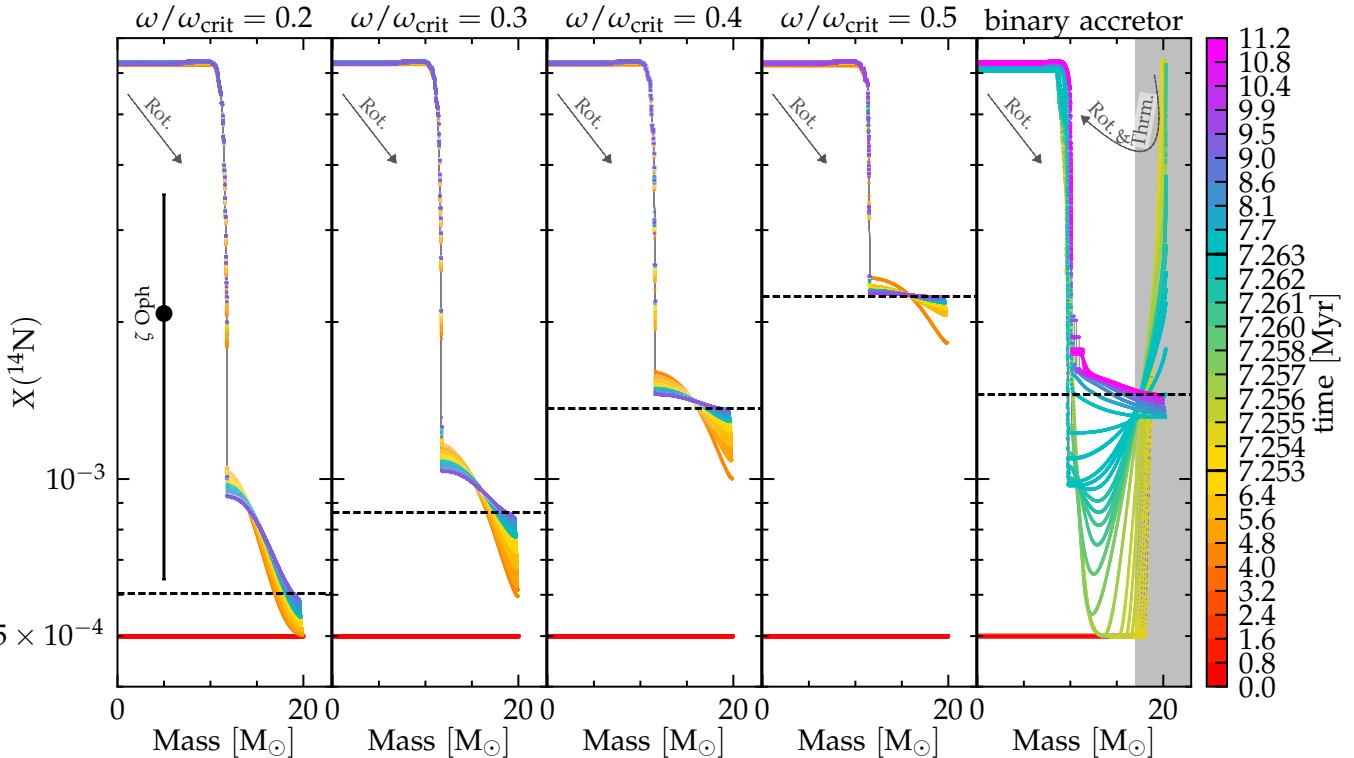


**Figure 4.**  $^{14}\text{N}$  mass fraction as a function of mass coordinate for  $20 M_\odot$  single star models with increasing  $\omega/\omega_{\text{crit}}$  at birth (first four panels), and for the accretor of our fiducial binary (last panel). The colorbar is non-uniform and allows for more color variation during RLOF. In each panel, the red flat line marks the primordial value for  $Z = 0.01$ , the thin dashed black line marks the surface value at TAMS. In the last panel, the gray area highlights mass accreted during RLOF. The black errorbar in the first panel shows the surface  $^{14}\text{N}$  of  $\zeta$  Oph estimated by VH05 assuming the surface mass fraction of H from Tab. 1. The abundance of  $^{14}\text{N}$  alone is not strongly constraining. Fig. 9 shows a similar plot containing also  $^{12}\text{C}$  and  $^{16}\text{O}$ .

Conversely, the  $^{14}\text{N}$  mass fraction profile of the accretor is *not* monotonic throughout the evolution. The profile is shaped by two main processes: (i) accretion of CNO-processed material from the donor star mixed inwards by meridional circulations and thermohaline mixing (as indicated by the top right arrow in the last panel), (ii) outward mixing of the CNO-processed material from the accretor’s core caused by rotational mixing – as in the single stars – and rejuvenation.

Initially, the tidally synchronized accretor star rotates too slowly ( $\lesssim 3 \text{ km s}^{-1}$ ) for significant outward rotational mixing out of the core, and until the onset of RLOF (roughly at 7.25 Myr) no appreciable variation of the envelope  $^{14}\text{N}$  mass fraction occurs. During late RLOF after the “kink” feature between C and D in Fig. 1, N-enriched material from the donor’s core

piles onto the accretor’s surface – inside the gray area. The close-to-critical rotation (through Eddington-Sweet circulations) and the inversion in the mean molecular weight  $\mu$  (through thermohaline mixing) drive inward mixing of the N-rich material and dilute it in the envelope (see also Fig. 3).

Simultaneously, the mere growth in mass causes the steepening of the core-temperature gradient and increase in the convective core mass (rejuvenation, e.g., Schneider et al. 2016), driving some outward convective mixing of N-rich material. This also causes the formation of an off-center convective region (cf. Fig. 3) which persists until TAMS. Because convection turnover timescale is much shorter than evolutionary timescales, convection homogenizes the composition of this region

and produces “steps” at the outer edge of the core (slightly outside mass coordinate  $10 M_{\odot}$ ).

In Fig. 4, the black errorbar in the first panel shows  $\zeta$  Oph’s surface  $^{14}\text{N}$  from VH05 (assuming the surface H mass fraction from our model listed in Tab. 1). The mass fraction of  $^{14}\text{N}$  alone is not sufficient to distinguish between these models, and already a moderate  $\omega/\omega_{\text{crit}} \geq 0.3$  is sufficient for models to reach the lower-limit of the error bar.

### 3.2. Angular momentum transport and surface rotation

One of the main distinguishing features of  $\zeta$  Oph is its extremely high surface rotation rate. The black line in the top panel of Fig. 5 shows the evolution of the surface equatorial rotational velocity  $v_{\text{eq}}$  for our accretor model, not including any projection effect. More precisely,  $v_{\text{eq}}$  is a mass-weighted average of the rotational velocity of layers with opacity  $\tau \leq 100$ . The dark horizontal red band corresponds to the  $v \sin(i) = 432 \pm 16 \text{ km s}^{-1}$  measured by Zehe et al. (2018), and the lighter band shows a range of 5 times their error bar, which roughly encloses the majority of the estimated  $v \sin(i)$  for  $\zeta$  Oph in the literature down to  $\sim 350 \text{ km s}^{-1}$ . For comparison, the colored solid lines show also  $v_{\text{eq}}$  for single rotating  $20 M_{\odot}$  stars of varying initial  $\omega/\omega_{\text{crit}}$ . The bottom panel of Fig. 5 shows instead the ratio of the surface rotational frequency  $\omega_{\text{surf}}$  to  $\omega_{\text{crit}}$ .

The initial binary is wide enough that assuming tidal synchronization at ZAMS implies a very low  $v_{\text{eq}} \lesssim 3 \text{ km s}^{-1}$ . At 7.25 Myr, RLOF rapidly spins up the accretor to critical rotation, up to  $\sim 520 \text{ km s}^{-1}$ . This corresponds to  $\omega/\omega_{\text{crit}} \simeq 0.95$  (dashed horizontal line in the bottom panel of Fig. 5), which is the upper-limit we impose in our models.

The star remains fast rotating throughout the mass transfer phase, which ends at the blue diamond in Fig. 5. In the remaining evolution, the star spins down progressively through wind mass loss, and within  $\sim 2$  Myr its averaged surface rotational velocity drops below  $\sim 350 \text{ km s}^{-1}$ . Both the single star models and our accretor (after being spun up) evolve to higher  $\omega/\omega_{\text{crit}}$  because of the increase in stellar radii and corresponding decrease in  $\omega_{\text{crit}}$  (e.g., Langer 1998; Zhao & Fuller 2020). However, our accretor remains at a higher  $\omega_{\text{surf}}/\omega_{\text{crit}}$  for a significantly longer time: the chance of observing a single rotating star at very high  $\omega_{\text{surf}}/\omega_{\text{crit}}$  is lower than for an accretor from a massive binary system. Close to the end of the main sequence, the increase in wind mass loss rate and internal transport of angular momentum strengthen the surface spin-down. This effect is also seen in the late main-sequence evolution of single stars rotating rapidly from ZAMS.

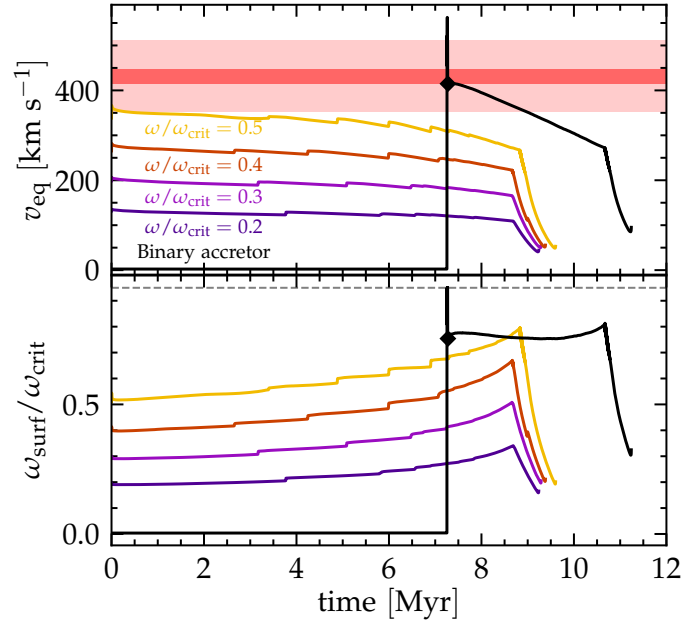


**Figure 5.** Equatorial surface rotational velocity (top panel) and  $\omega/\omega_{\text{crit}}$  (bottom panel) for the accretor model (black) and single rotating  $20 M_{\odot}$  stars (colored lines). At  $\sim 7.25$  Myr the mass transfer quickly spins up the accretor to critical rotation: the dashed horizontal line in the bottom panel shows the upper-limit we impose. By the time the donor detaches from the RLOF the accretor is still spinning at  $\sim 400 \text{ km s}^{-1}$ . From this point (blue diamonds) onwards, we continue the evolution as a single star, and the accretor spins down because of wind mass loss. Note however that we use the wind mass-loss rate from Vink et al. (2001), which might be  $\sim 2$  orders of magnitude too high for  $\zeta$  Oph (Marcolino et al. 2009).

Fig. 5 shows that our model can retain a significant surface rotation for a time comparable to the kinematic age of the star, which is shorter than the remaining main-sequence lifetime. Since the spin up of the accretor happens roughly half-way through its main-sequence, the star is much faster rotating than single stars of the same (post-RLOF) mass initialized as fast rotators at ZAMS. Although Fig. 5 does not account for the projection angle, Zehe et al. (2018) argued for  $i \geq 56$  degrees, corresponding to an upward shift of the red band in Fig. 5 of  $\lesssim 20\%$ . This has the same impact on our accretor model and on single star models of  $\zeta$  Oph.

We emphasize that our model is computed using the Vink et al. (2000, 2001) wind mass-loss rate with full efficiency throughout its evolution. This is two orders of magnitude higher than the wind mass loss rate reported by Marcolino et al. (2009) (weak wind problem, however, see also Lucy 2012; Lagae et al. 2021). While this may impact the evolution of the binary even before RLOF, it presumably increases the spin-down rate of our

model compared to the observations. We expect that an accreting star modeled with lower wind-mass loss rate post-RLOF would retain an even higher surface rotation for longer (see also Sec. 4.1).

### 3.2.1. Comparison to single fast-rotating stars

To illustrate the angular momentum transport in our accretor stars, it is again helpful to compare with single rotating  $20 M_{\odot}$  models. Typically, single stars are assumed to be solid-body rotators at ZAMS. As they contract and lose mass, their internal rotational profile evolves differently than the profile obtained spinning up the secondary star at a later on, from its surface, and to critical rotation.

The top row of Fig. 6 shows the internal rotational velocity  $v_{\text{rot}} = \omega \times r$ , while the bottom row shows the  $\omega$  profile. As in Fig. 4, the first four panels in each row show single rotating stars with increasing initial  $\omega/\omega_{\text{crit}}$ , the last panels shows our accretor model.

The thin horizontal dashed black lines in each panel of the top row of Fig. 6 mark the TAMS surface rotation rates: all our single star models reach a TAMS surface  $v_{\text{rot}} \simeq 50 - 60 \text{ km s}^{-1}$ . Initially faster rotating models spin down more in their outer layers, have slightly longer main sequence lifetimes (because of rotational mixing increasing the available fuel), and develop stronger differential rotation. As the core contracts and spins up, the single star profiles show the progressive development of a core-envelope interface.

Conversely, the last panel shows that the entire interior of the accretor has a negligible rotational velocity until RLOF (starting at  $\sim 7.25$  Myr). Because of binary interactions, the accretor is spun up late in its evolution, up to critical rotation  $\omega/\omega_{\text{crit}} \simeq 1$ , and from the surface. In our model, inward transport of angular momentum creates a  $v_{\text{rot}}$  profile monotonically increasing from the center to the surface. After the end of mass transfer, roughly at 7.27 Myr, the accretor achieves rigid and close to critical rotation (flat profiles in the last panel on the bottom row of Fig. 6). At the end of our binary run, the accretor is still rigidly rotating, and persists<sup>5</sup> for a total duration of  $\sim 10^4$  years. Afterwards, the accretor's envelope spins down because of winds. By the end of the main-sequence evolution of the accretor, the surface still spins with  $v_{\text{rot}} \simeq 100 \text{ km s}^{-1}$  (twice as fast as the single star models).

Perhaps more importantly, the outer-edge of the core has a similar rotational velocity as the surface, and a

much larger rotational frequency than the cores of single star models. This is because the evolutionary contraction (decrease in  $r$ ) of the core results in a significant increase of  $\omega$  to conserve the angular momentum that cannot be efficiently transferred to the outer layers. The core-envelope interface in the rotation profile of the accretor at TAMS is much more prominent than in single rotating stars. The higher core spin of accretors spun-up late and up to critical rotation might have important implications for the explosion of the accretors, the spin of the resulting compact objects, and the analysis of gravitational-wave events (e.g., Zaldarriaga et al. 2018; Qin et al. 2018; Callister et al. 2020).

## 4. ROBUSTNESS OF THE MODELS AND DISCUSSION

Models of the interior evolution of stars require the choice of several poorly constrained parameters, most arising from the one-dimensional representation of multi-dimensional phenomena (convection, mixing, rotation, etc.). This remains true when modeling two stars in a binary, with the added caveat that an even larger number of parameters enters in the treatment of binary interactions (and in particular mass transfer). This emphasizes the need for observational constraints and motivated us to compare our models to the observationally well characterized  $\zeta$  Oph.

Accretor stars are expected in most populations of (massive) stars, both in clusters (e.g., Chen & Han 2009; Wang et al. 2020) and in the field (e.g., de Mink et al. 2011, 2013). However, these might not obviously stand out as binary products in kinematics surveys (e.g., Renzo et al. 2019). Therefore, to inform the search for accretor stars in observed samples, it is also necessary to characterize the robustness of model predictions against numerical, physical, and algorithmic choices. In Sec. 4.1 we report on exploration of parameter variations for each individual star in the binary. We discuss parameters governing the mass transfer phase in Sec. 4.2, the initial binary architecture in Sec. 4.3, and the consequences of the assumed SN explosion of the companion in Sec. 4.4.

### 4.1. Uncertainties in the single-star physics

Rotation is a critical ingredient of our models: it governs the equatorial radius and thus  $\omega/\omega_{\text{crit}}$ . Therefore by assumption it also controls the mass transfer efficiency through mechanical enhancement of the accretor's wind (see Sec. 4.2). Through Eddington-Sweet meridional circulations, rotation determines outward mixing from the core, and more importantly inward mixing from the surface. We emphasize that the shellular approximation used in one-dimensional stellar evolution codes might

<sup>5</sup> To calculate the duration, we consider rotation to be rigid if the difference between the minimum and maximum frequency throughout the star is  $\Delta\omega \lesssim 10^{-2} \text{ days}^{-1}$ .

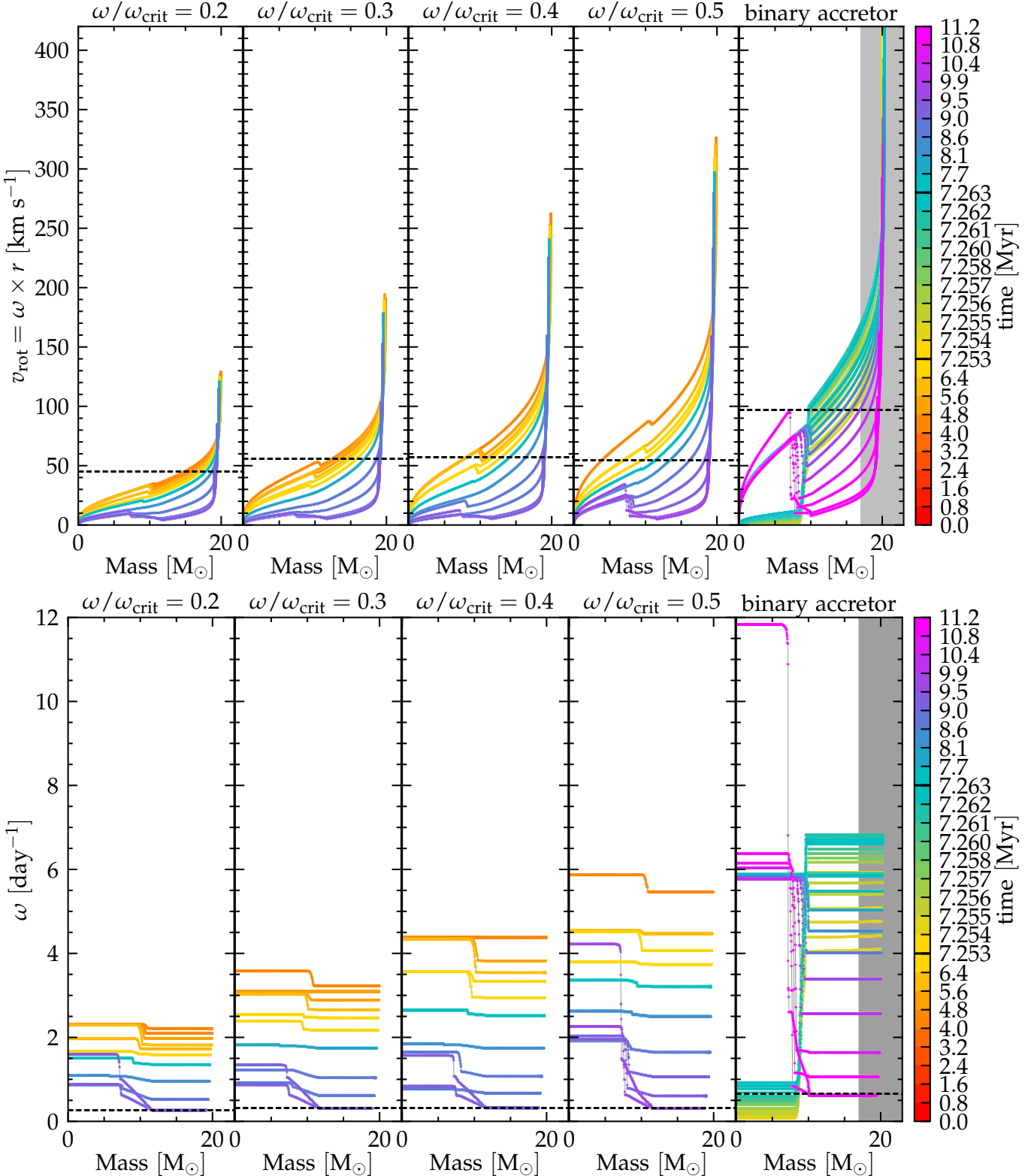


**Figure 6.** Top: Internal rotational profile for  $20 M_{\odot}$  single star models with increasing  $\omega/\omega_{\text{crit}}$  at birth (first four panels), and for the accretor of our fiducial binary. Bottom: internal rotational frequency profile. As in Fig. 4, the colorbar is non-uniform. In the top (bottom) panel the thin dashed black line mark the TAMS surface rotation rate (surface rotation frequency). In the rightmost panels, the gray areas indicate mass accreted during RLOF. The pink lines (TAMS) in the last panel show that the core of the accretor is rotating almost as fast as its surface despite its much smaller radius, and both are faster than the surface of single star models.

not be appropriate for  $\omega/\omega_{\text{crit}} \simeq 1$  reached by our accretor star during RLOF. Decreasing by a factor of 10 the diffusion coefficient for Eddington-Sweet meridional circulations has a very small effect on the evolution of the accretor on the HR diagram. However, the noisiness during the late RLOF phase (beyond point B in Fig. 1) increases in amplitude, confirming that the details of this part of the evolution are sensitive to the treatment of rotational mixing (and its interplay with other processes).

Our models assume a Spruit-Tayler dynamo (Spruit 2002) for the transport of angular momentum throughout the evolution. Adopting the stronger angular momentum transport from Fuller et al. (2019) might result in a more efficient spin-down of the surface during RLOF, possibly allowing for more accretion of mass.

The accretor is spun up late, from the surface inwards, and to critical rotation compared to single star models which are initialized at ZAMS with rigid rotation. Late during the mass transfer, even the weak core-envelope coupling of Spruit (2002) is sufficient for the accretor to achieve rigid rotation. Subsequently, the envelope spins down because of wind mass loss and more importantly the core spins significantly up because of its evolutionary contraction. We expect that following Fuller et al. (2019) the core would lose more angular momentum to the envelope, limiting its ability to spin up as it contracts and decreasing its rotational velocity. Nevertheless, we expect that the difference with single star rotational profiles would remain because of the shorter evolutionary time left.

During RLOF, thermohaline mixing in the envelope also becomes important. In MESA, each mixing process is represented by its own diffusion coefficient, and they are then summed together (e.g., Paxton et al. 2011), under the implicit assumptions that mixing processes are independent from each other. This is typically reasonable since locally one process dominates the mixing.

In the envelope of our accretor model, initially Eddington-Sweet circulations are dominant, however thermohaline mixing reaches and exceeds their diffusivity late during the mass transfer. If fast rotation can physically modify thermohaline mixing processes, this might impact our accretor models. We also tried models enhancing the efficiency of thermohaline mixing by a factor of 100 (Schootemeijer et al. 2019) but these proved numerically unstable when accreting CNO-processed material.

We have also explored models with a step overshooting following Brott et al. (2011). Our fiducial exponential overshooting was chosen to reproduce the width of the main-sequence of the models of Brott et al. (2011), and

not-surprisingly, the qualitative evolution of our fiducial model and models with step overshooting is similar. However, adopting a step overshooting provides a higher diffusivity at the outer edge of the core (cf. exponential decrease) which ultimately impacts the details of the chemical profile at the outer edge of the core, and the morphology of the evolutionary tracks during late RLOF.

$\zeta$  Oph is one of the low-luminosity O-type stars for which Marcolino et al. (2009) found a lower-than-predicted mass loss rate. To address the “weak wind problem”, we also attempted running models with artificially decreased wind mass loss rate (e.g., Renzo et al. 2017), but these resulted in super-critical  $\omega/\omega_{\text{crit}} > 1$  post-RLOF accretor stars with untrustworthy numerical results. The solution to the “weak wind problem” is not currently known, but Lucy (2012) and Lagae et al. (2021) suggest that observed mass loss rates might be underestimated.

Throughout Sec. 3, we assumed an initial metallicity  $Z = 0.01$  informed by the asteroseismology of low mass stars in the parent association Upper-Centaurus-Lupus (e.g., Murphy et al. 2021). Moreover, we have assumed that mass fractions of each element scale with the Solar values (Grevesse & Sauval 1998), which might not be appropriate especially for massive stars (e.g., Grasha et al. 2021). With these assumptions, the initial mass fraction of  $^{12}\text{C}$  and  $^{14}\text{N}$  are lower than the values reported by VH05 for  $\zeta$  Oph. Even though both values increase during mass transfer, our model still slightly under-predicts them. Improved agreement could be obtained changing the ratio of abundances to non-solar values, or by changing the efficiency of downward rotational and thermohaline mixing which dilutes the accreted material into the secondary’s envelope.

We also run a model identical to the one described in Sec. 3, except with  $Z = Z_{\odot} = 0.0142$  (Asplund et al. 2009). Qualitatively, the binary evolution remains similar, with the higher metallicity stars having slightly larger radii and cooler  $T_{\text{eff}}$  at a given luminosity. This still produces a stable case B RLOF, however, the accretor track is displaced on the right on the HR diagram. Thus, matching the high present-day  $T_{\text{eff}} = 32\,000 \pm 2\,000$  of  $\zeta$  Oph (e.g., VH05) requires more massive and hotter accretors at higher  $Z$  (see also Sec. 4.3).

#### 4.2. Uncertainties in the treatment of mass transfer

We regulate the accretion efficiency through the rotational enhancement of mass loss (e.g., Langer 1998). However, whether critical rotation can effectively stop the accretion of matter is unclear. Popham & Narayan

(1991) and Paczynski (1991) argued that accretion of mass (but not angular momentum) might be possible even at or beyond critical rotation.

During RLOF, the total amount of mass lost by the donor is  $\Delta M_{\text{donor}} \simeq 10.6 M_{\odot}$ , of which only  $\Delta M_{\text{accretor}} \simeq 3.4 M_{\odot}$  are successfully accreted by the companion. This corresponds to an overall mass transfer efficiency  $\beta_{\text{RLOF}} \equiv |\Delta M_{\text{accretor}}|/|\Delta M_{\text{donor}}| \simeq 0.32$ , although the accretion efficiency is *not* constant throughout the mass transfer (e.g., van Rensbergen et al. 2006). In our models, the mass transfer efficiency depends on the radial and rotational evolution of the accreting star. During RLOF, the accretor is out of gravothermal equilibrium with significant impact on its radius and ultimately on the amount of mass transferred and its angular momentum. In reality, the gas stream between the two stars, the hot-spot due to the RLOF stream hitting the accretor's surface (see below), and the geometric distortion of the outer layers because of the centrifugal forces would not follow the spherical symmetry imposed by 1D codes such as MESA.

While the mass transfer efficiency  $\beta_{\text{RLOF}}$  and importantly its time-evolution need further attention, it is also likely that this parameter and its evolution depend on the details of the system (masses, mass ratio, period, etc.). For instance, to explain the lower mass sdO+Be binaries found by Wang et al. (2021) it is likely that a larger mass transfer efficiency would be required.

Most studies, especially using rapid population synthesis tools, typically assume a constant  $\beta_{\text{RLOF}}$  and neglect the out-of-equilibrium phase of the accretor and how this can impact the binary and orbital evolution. Alternatively, rapid population synthesis can limit the accretion rate based on the thermal timescale of the accretor (calculated from models in gravothermal equilibrium). Based on this approach, Schneider et al. (2015) found a higher  $\beta_{\text{RLOF}} \simeq 0.7$  for a binary comparable to ours (initially  $M_1 = 20 M_{\odot}$ ,  $M_2 = 0.7M_1$  with separation  $a \simeq 300 R_{\odot}$ ), although their  $\beta_{\text{RLOF}}$  is very sensitive to the initial mass ratio and period in this regime.

Another free parameter in the treatment of mass transfer is the specific angular momentum of the accreted material. This is an uncertain quantity and likely depends on the geometry of the accretion process, and in particular, whether the accretion stream through the L1 Lagrangian point hits directly the accretor star, or if instead an accretion disk is formed (e.g., de Mink et al. 2013).

We calculate the minimum distance  $R_{\min}$  between the stream coming from the L1 Lagrangian point and the accretor using the fit from Ulrich & Burger (1976) to the numerical results of Lubow & Shu (1975). We find

$R_{\min} \simeq 1.5 R_{\odot} < R_{\text{accretor}}$ : this suggests that the stream should directly hit the accretor, without forming an accretion disk. Nevertheless, for the sake of numerical stability, we assume the incoming material and the stellar surface to have the same specific angular momentum. This provides a slow angular momentum accretion and consequent spin-up of the surface.

We also attempted calculations using for specific angular momentum of the accreted material  $j = \sqrt{1.7GM_{\text{accretor}}R_{\min}}$ , representative for direct impact of the incoming stream with the accretor (Lubow & Shu 1975). This is typically much larger than the specific angular momentum of the accretor's surface. However, these models proved numerically more unstable and providing less trustworthy results after the accretor is spun up significantly. In general, allowing for a faster accretion of angular momentum results in a faster spin-up, and a lower overall mass transfer efficiency  $\beta_{\text{RLOF}}$ .

In our models, the composition of the transferred material is determined by the structure of the donor and the mass transfer rate calculated following Kolb & Ritter (1990), but we need to specify its specific entropy when it reaches the accretor surface. We follow the common practice of assuming the specific entropy of the incoming material to be same as the accreting surface. The scenario justifying this hypothesis is that during RLOF the matter is sufficiently optically thin so that radiative processes can rapidly equalize the entropy between the RLOF stream and the accreting surface. However, the very large mass-transfer rates we find (cf. Fig. 2) might result in optically thick flows for which this approximation might not be appropriate.

Because of the increase in mass, our accretor star is rejuvenated: its total main-sequence lifetime is longer than the lifetime of a single star born with the final post-RLOF mass of the accretor<sup>6</sup> (e.g., Schneider et al. 2016). The rejuvenation is due to the increase - in mass - of the core region, which brings inward fresh nuclear fuel. Our results are in agreement with Hellings (1983), while Braun & Langer (1995) did not find any rejuvenation in their accretor models. We attribute this difference to the lack of convective boundary mixing (e.g., overshooting, efficient semiconvection, shear) in their models, which impedes the growth of the core.

In our models, the growth of the core is initially driven by convection and overshooting, and to a lesser extent to dynamical shear. Later on, a convective region above the overshooting region develops (third panel onwards

<sup>6</sup> But not significantly longer than the lifetime of a single star of its initial, pre-RLOF mass.

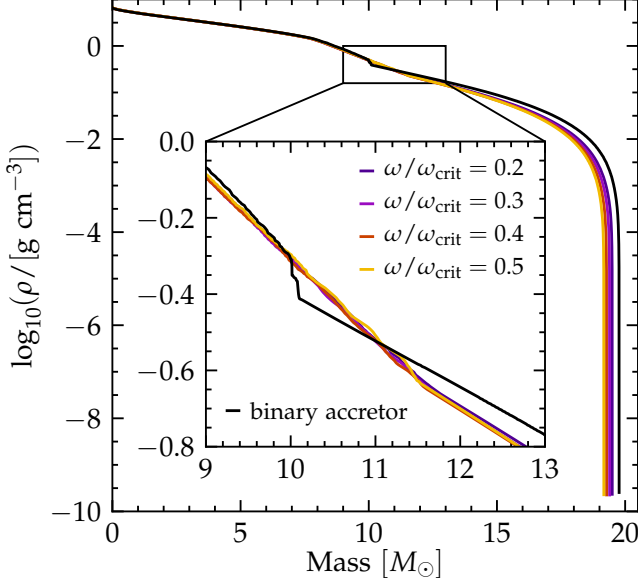


**Figure 7.** Comparison of the density profiles of the accretor model (black) and single  $20 M_{\odot}$  rotating stars (colors). The models are compared when they reach the same central H mass fraction of  $X_c = 0.085$  (point G in Fig. 1 for the accretor). The inset magnifies the region above the core, where the outcome of common envelope events is decided. Because of the growth of the core, the density profile of the accretor in this region is significantly different.

in Fig. 3) and remains as an off-center feature until and beyond point G in Fig. 1, however, this convective region is not efficiently mixed with the core: although its appearance is a consequence of accretion, it does not contribute directly to the increase in available fuel.

Fig. 7 shows a density comparison between the accretor in the last panel of Fig. 3 and four initially  $20 M_{\odot}$  single rotating stars. The off-center convective region significantly alters the density profile above the core of the accretor compared to a single star. The sharper inner density drop and shallower density profile of accretors might be probed with asteroseismology:  $\zeta$  Oph itself has been observed to show non-radial pulsations (Walker et al. 2005), which may be involved in the transient appearance of emission lines and a decretion disk. If compared to a star of comparable mass which evolved as single, the pulsations could shed light on the structural differences between single stars and binary products.

Moreover, if the binary system remains bound after the explosion of the donor and the evolutionary expansion of the accretor leads to a common envelope (e.g., Paczynski 1976), the layer above the He core is crucial to determine the success or failure of the common envelope ejection. Although this is not the future fate of  $\zeta$  Oph, this might be crucial for our understanding of

gravitational wave progenitors. Common envelope simulations have so far neglected the impact of previous RLOF phase(s) on the density structure of the stars initiating the dynamically unstable mass transfer.

#### 4.3. Variations in initial binary parameters

The initial donor mass  $M_1$ , mass ratio  $q = M_2/M_1$ , and the period of the progenitor binary of  $\zeta$  Oph cannot be directly constrained from observations. We have explored variation in these values, and the qualitative behavior of the models is similar. Shorter initial periods results in larger post-RLOF orbital velocities, and thus larger runaway velocities if the binary is disrupted at the first SN (see Sec. 4.4). For example, taking  $P=75$  days (cf. 100 days in our fiducial model in Sec. 3), the binary still experiences stable case B mass transfer, but the post-RLOF orbital velocity of the accretor is about  $60 \text{ km s}^{-1}$ , that is  $\sim 10 \text{ km s}^{-1}$  higher than in our fiducial model.

Increasing the donor mass also has a similar effect on the post-RLOF orbital velocity of the accretor. Using  $M_1 = 30 M_{\odot}$  (cf.  $25 M_{\odot}$  in Sec. 3),  $M_2 = 17 M_{\odot}$ , and  $P=100$  days, we obtain a post-RLOF velocity of  $65 \text{ km s}^{-1}$ . However, this produces a stripped donor of  $\sim 16 M_{\odot}$  at RLOF detachment, with stronger wind mass loss. Therefore this binary is expected to widen relatively more than our fiducial model of Sec. 3, slowing down the accretor. The increased mass of the stripped star could also imply a lower chance of exploding for the donor, which might instead collapse to a black-hole instead (however, see Sec. 4.4).

The higher  $M_1$  does not significantly change the post-RLOF total mass of the accretor, with  $M_2$  remaining about  $\sim 20.5 M_{\odot}$ , since in our models accretion is regulated mostly by the spin up of the accretor, and we do not couple the specific angular momentum of the transferred material to the orbit or the donor’s spin.

However, changing the initial mass ratio also changes the difference between the main-sequence lifetime of the two stars, and thus how far along the main sequence the accretor is at the onset of RLOF. The observed position of  $\zeta$  Oph on the HR diagram, particularly its relatively high  $T_{\text{eff}}$  are difficult to reproduce assuming initially less massive accretors (which would remain too cool even after accreting mass), or more equal initial mass ratio (which would produce an accretor that is too evolved and cool at the onset of mass transfer).

#### 4.4. The explosion of the donor star

Throughout this study, we have assumed the “binary SN scenario” to explain the runaway nature of  $\zeta$  Oph: after the mass transfer phase, the explosion of the donor

disrupts the binary and ejects the accretor at roughly its pre-explosion orbital velocity (e.g., Blaauw 1961; Renzo et al. 2019). This fate occurs to the majority of massive binary systems, and  $\zeta$  Oph might be the best example of it (e.g., Blaauw 1952, 1961; Hoogerwerf et al. 2000). Neuhäuser et al. (2020) suggested not only the companion successfully exploded producing the pulsar PSR B1706-16 and ejecting  $\zeta$  Oph, but also that the explosion produced radioactive  $^{60}\text{Fe}$  which polluted Earth.

From kinematic and orbital considerations they estimated the pulsar received a natal kick of  $253 \pm 54 \text{ km s}^{-1}$ , which would be sufficiently large to unbind the binary which has  $v_{\text{orb}} = \sqrt{G(M_1 + M_2)/a} \simeq 135 \text{ km s}^{-1}$  at the end of our binary simulation (blue diamond in Fig. 1) and this will decrease further in the remaining time to the donor’s core-collapse (Kalogera 1996; Tauris 2015).

The SN ejecta mass would depend on the post-RLOF wind mass loss of our donor star, which is very uncertain (e.g., Renzo et al. 2017; Vink 2017; Gilkis et al. 2019). At the end of our binary evolution simulation, our stripped donor is  $\sim 9.4 M_\odot$ , with a surface H fraction of  $X \lesssim 0.2$  for a layer of  $\Delta M \simeq 2.5 M_\odot$ . Its wind mass-loss rate is  $\sim 10^{-5} M_\odot \text{ yr}^{-1}$  (Nugis & Lamers 2000, see also Fig. 2), likely to increase as it contracts and increases its luminosity and effective temperature. We expect its explosion to appear as H-less type Ib SN. Although our stripped donor is rather massive, recent studies hints at a higher “explodability” of donor stars in binary systems (e.g., Schneider et al. 2021; Laplace et al. 2021; Vartanyan et al. 2021).

We have neglected the impact of the explosion on the structure of the accretor star. At the time of the explosion, the accretor subtends a solid angle  $\sim R^2/a^2 \simeq 2 \times 10^{-3}$  steradians with  $R$  the accretor radius and  $a$  the binary separation. We neglect the post-RLOF wind-driven orbital widening for this estimate. The blast wave will hit the accretor causing mass loss – directly via ablation and by injecting energy in the envelope, inflating it and enhancing its wind (Wheeler et al. 1975; Tauris & Takens 1998; Podsiadlowski 2003; Hirai et al. 2018). Because of the SN shock, the just ejected new runaway star might appear bloated and redder (long before it overtakes the slowing SN remnant). The impact of this brief out of thermal equilibrium phase on the stellar spin should be investigated further.

Using 2D hydrodynamic simulations of the star-SN ejecta interactions in close binaries ( $a \lesssim 60 R_\odot$ , cf.  $a \gtrsim 343 R_\odot$  in our fiducial binary model), Hirai et al. (2018) found that the companion star recovers its pre-explosion luminosity and effective temperature within a few years to decades, and the amount of mass removed by the SN

shock is  $\lesssim 10^{-2} M_\odot$ . The SN ejecta might also pollute the surface of the runaway depositing processed nuclear material (e.g., Przybilla et al. 2008; Suda et al. 2021). However, for the large final separation of our model, little pollution is expected and enhanced mass loss and inward mixing might quickly dilute any signature below detectable levels.

## 5. SUMMARY & CONCLUSIONS

The impact of mass transfer on the structure and evolution of accretor in massive binaries has received relatively little attention in the literature. To investigate this, we have performed **MESA** calculations of massive binaries evolving two coupled stars simultaneously.

As a first application, we focused on finding a model in which the accretor properties are in qualitative agreement with observations of the nearest O-type star to Earth. This is the runaway  $\zeta$  Oph, which has long been suggested to be a former accretor star ejected from a binary at the core-collapse of the donor star (binary SN scenario, Blaauw 1961). However, our models are also informative for the generic population of massive accretors.

### 5.1. Reproducing $\zeta$ Oph

We found that the main features of  $\zeta$  Oph can be reasonably well reproduced using standard stellar physics assumptions for the treatment of mass transfer, chemical mixing, and rotation. Our choices are described in Sec. 2 and Appendix A.

Our fiducial model is a binary starting with  $M_1 = 25 M_\odot$ ,  $M_2 = 17 M_\odot$ , and  $P = 100$  days at metallicity  $Z = 0.01$  (see Sec. 3). This binary experiences stable thermal-timescale Roche lobe overflow after the end of the main sequence of the donor (case B).

The accretor compares well with observations of  $\zeta$  Oph about  $1.5 - 2$  Myrs after the end of mass transfer, corresponding to the remaining donor’s lifetime at the end of our simulations plus the kinematic age of  $\zeta$  Oph. Specifically, the position on the HR diagram (cf. Fig. 1), the runaway space velocity (estimated based on the accretor’s orbital velocity), the surface composition and rotational velocity (cf. Tab. 1) are in the right ballpark.

Our model of  $\zeta$  Oph differs significantly from previous studies: in contrast with the accretor models of van Rensbergen et al. (1996), in our model the  $^{14}\text{N}$ - and  $^4\text{He}$ -rich surface composition is not the result of pure outward rotational mixing. Instead, this material is transferred from the receding core of the donor star and mixed from the surface inwards into the accretor by meridional circulations and thermohaline mixing. Thus, the present day surface mass fractions of  $\zeta$  Oph place a coupled constraint on the mass transfer efficiency and mixing in

the accretor. Our results suggest  $\zeta$  Oph should not be used to calibrate models of rotational mixing in single star models.

We emphasize that the surface composition alone would not be a smoking-gun, especially given the large uncertainties in the treatment of rotation and mixing in stellar evolution models. In our models, the accretion of  $^{14}\text{N}$  from the donor allows the accretor to be simultaneously fast rotating and  $^{14}\text{N}$ -rich, while single rotating stars can only mix upward  $^{14}\text{N}$  from their core, and have significantly spun down by the time they become  $^{14}\text{N}$ -rich. Moreover, alternative scenarios where  $\zeta$  Oph evolved as a single fast-rotating star require ad-hoc explanations for the runaway velocity, and have been shown by VH05 to struggle in reproducing surface mass fractions, apparent age, mass, and rotation rate simultaneously.

The surface rotation rate of the accretor post-mass-transfer is always higher than the rotation rate of single stars initialized with half-critical rotation, but might still be on the low side compared to  $\zeta$  Oph. However, the wind spin down might be overestimated in our models (weak wind problem).

We also tested the robustness of our fiducial model against variations in the initial parameters and algorithmic representation of physical phenomena, discussed in Sec. 4. Less massive accretors remain too cool throughout the evolution to be compatible with  $\zeta$  Oph, and initial mass ratios closer to unity lead to a more evolved accretor at the onset of mass-transfer, again resulting in too cool temperatures. Increasing the donor's initial mass might result in stripped stars unlikely to form a neutron star in their final SN explosion.

### 5.2. Accretors are not single rotating stars

Our models also highlight some general differences between accretors in massive binaries and stars evolving as single throughout their life. These have been so far under-appreciated but might be important for several sub-fields of astrophysics, including asteroseismology, stellar populations, and time-domain and gravitational waves observations.

The first notable difference we find is the internal rotation profile. Single rotating stars are usually initialized as rigid rotators at birth, and throughout their evolution they spin down to wind mass loss. Conversely, accretors are spun up later (roughly half-way through the main sequence in our model from Sec. 3), and from the surface. Moreover, for single stars the maximum rotation rate, that is the one assumed at the beginning of the

evolution, is poorly understood theoretically or observationally (e.g., Ramírez-Agudelo et al. 2013; Ramírez-Agudelo et al. 2015). Conversely, accretors in binaries reach critical rotation  $\omega/\omega_{\text{crit}} \simeq 1$ . The later spin-up and higher rotation achieved allow the accretor star to remain a fast rotator until the end of its main sequence.

The angular momentum accreted at the surface of the accretor is transported into the core (by the Spruit-Tayler dynamo in our simulations). This results in a much faster rotating helium core at the end of the main sequence compared to single stars, with potential implications for the final explosion and the resulting compact object born from the accretor star in an interacting binary system.

Finally, in our models, the accretion of mass and consequent rejuvenation of the accretor leads to a different density profile at the bottom of the envelope. The details of the difference are likely sensitive to what allows the core to grow and the rejuvenation to happen. In our models, the growth of the core leads to an off-center convective shell (cf. Fig. 3 and Fig. 7). This shell results in a sharper density drop at the core edge, and a flatter density profile close to the end of the main sequence. This could in principle be probed by asteroseismology. Depending on how the accretor (and the binary) evolves in the future, this difference could be crucial in determining the outcome of common envelope events between massive stars and compact objects.

Improving our understanding of the evolution of the initially less massive stars in massive binary systems is crucial for the upcoming large surveys, stellar kinematics, and for the understanding of the evolution of gravitational-wave progenitors in isolated binaries. Although presently single, the nearest O-type star to Earth,  $\zeta$  Oph, can be used as an anchor point for the modeling of accretors. Our models demonstrate that a broad agreement with observations can be achieved with standard stellar evolution assumptions. Future efforts should extend these models to a wider mass, period, mass ratio, and metallicity range to investigate the impact of binary evolution on the life, explosion, and after-life of the secondary stars in massive binary systems.

*Software:* MESA (Paxton et al. 2011, 2013, 2015, 2018, 2019), mesaSDK (Townsend 2018), ipython/jupyter (Pérez & Granger 2007), matplotlib (Hunter 2007), mesaPlot (Farmer 2018), NumPy (van der Walt et al. 2011).

### A. MESA SETUP

We use `MESA` version 15140 to compute our models. The `MESA` equation of state (EOS) is a blend of the OPAL [Rogers & Nayfonov \(2002\)](#), SCVH [Saumon et al. \(1995\)](#), PTEH [Pols et al. \(1995\)](#), HELM [Timmes & Swesty \(2000\)](#), and PC [Potekhin & Chabrier \(2010\)](#) EOSes.

`OPAL` ([Iglesias & Rogers 1993, 1996](#)) provides the main radiative opacities, with low-temperature data from [Ferguson et al. \(2005\)](#) and the high-temperature from [Buchler & Yueh \(1976\)](#). Electron conduction opacities are from [Cassisi et al. \(2007\)](#).

Nuclear reaction rates are a combination of rates from NACRE ([Angulo et al. 1999](#)), JINA REACLIB ([Cyburt et al. 2010](#)), plus additional tabulated weak reaction rates [Fuller et al. \(1985\)](#); [Oda et al. \(1994\)](#); [Langanke & Martínez-Pinedo \(2000\)](#). Screening is included via the prescription of [Chugunov et al. \(2007\)](#). Thermal neutrino loss rates are from [Itoh et al. \(1996\)](#). We use a 22-isotope nuclear network (`approx_21_plus_cr56`).

The inlists, processing scripts, and model output are available at <https://doi.org/10.5281/zenodo.4701565>.

### B. RESOLUTION TESTS

We extensively checked the numerical convergence of our stellar evolution calculations with increasing number of mesh points. Fig. 8 shows that all the main features described here do not vary when increasing the spatial resolution by increasing the number of mesh points (i.e., decreasing `mesh_delta_coeff`). The right panel shows the number of mesh points for the accretor (top) and

donor (bottom) as a function of the model number (akin to an arbitrary time coordinate). About  $\sim$ 7000 `MESA` models are used to compute the binary evolution. The higher resolution run has  $\sim$  20% more mesh points. The left panel shows the evolution on the HR diagram until the detachment of the binary for the two accretor models (pink/red) and the two donor models (blue/cyan).

Similarly, we tested the numerical convergence with decreasing timestep size. This can be done decreasing the parameter `mesh_time_coeff`. However, we were unable to successfully compute models at higher temporal resolution. Partial results show a good agreement with our fiducial model until `MESA` becomes unable to find a satisfying numerical solution to the stellar structure equations (typically during RLOF). Lower temporal resolution models showed a similar qualitative agreement but increased noisiness during the late RLOF phase. For our fiducial model the adaptive timestep size never exceeds  $10^{3.8}$  years with typical pre-RLOF timesteps of the order of  $10^{3.2}$  years and sub-decade (occasionally sub-year) during RLOF. The main factor limiting the timestep sizes is the change of surface angular momentum in both stars during the mass transfer.

### C. INTERNAL COMPOSITION PROFILE EVOLUTION

Fig. 9 compares the internal evolution of the composition profile of single rotating stars with our accretor model. We show mass fractions of  $^{12}\text{C}$  and  $^{16}\text{O}$  to complement the mass fraction of  $^{14}\text{N}$  shown in Fig. 4, and reproduced also in the middle panel of Fig. 9.

## REFERENCES

- Almeida, L. A., Sana, H., Taylor, W., et al. 2017, *A&A*, 598, A84, doi: [10.1051/0004-6361/201629844](https://doi.org/10.1051/0004-6361/201629844)
- Angulo, C., Arnould, M., Rayet, M., et al. 1999, *Nuclear Physics A*, 656, 3, doi: [10.1016/S0375-9474\(99\)00030-5](https://doi.org/10.1016/S0375-9474(99)00030-5)
- Arnett, W. D. 1969, *Ap&SS*, 5, 180, doi: [10.1007/BF00650291](https://doi.org/10.1007/BF00650291)
- Asplund, M., Grevesse, N., Sauval, A. J., & Scott, P. 2009, *ARA&A*, 47, 481, doi: [10.1146/annurev.astro.46.060407.145222](https://doi.org/10.1146/annurev.astro.46.060407.145222)
- Belczynski, K., Holz, D. E., Bulik, T., & O'Shaughnessy, R. 2016, *Nature*, 534, 512, doi: [10.1038/nature18322](https://doi.org/10.1038/nature18322)
- Blaauw, A. 1952, *BAN*, 11, 414
- . 1961, *BAN*, 15, 265
- Blaauw, A. 1993, in *Astronomical Society of the Pacific Conference Series*, Vol. 35, *Massive Stars: Their Lives in the Interstellar Medium*, ed. J. P. Cassinelli & E. B. Churchwell, 207
- Blagorodnova, N., Klencki, J., Pejcha, O., et al. 2021, arXiv e-prints, arXiv:2102.05662, <https://arxiv.org/abs/2102.05662>
- Bodensteiner, J., Baade, D., Greiner, J., & Langer, N. 2018, *A&A*, 618, A110, doi: [10.1051/0004-6361/201832722](https://doi.org/10.1051/0004-6361/201832722)
- Bodensteiner, J., Shenar, T., & Sana, H. 2020, *A&A*, 641, A42, doi: [10.1051/0004-6361/202037640](https://doi.org/10.1051/0004-6361/202037640)
- Bouquet, D., & Evans, N. W. 2018, <https://arxiv.org/abs/1804.05849>
- Braun, H., & Langer, N. 1995, *A&A*, 297, 483
- Broekgaarden, F. S., Berger, E., Neijssel, C. J., et al. 2021, arXiv e-prints, arXiv:2103.02608, <https://arxiv.org/abs/2103.02608>
- Brott, I., de Mink, S. E., Cantiello, M., et al. 2011, *A&A*, 530, A115, doi: [10.1051/0004-6361/201016113](https://doi.org/10.1051/0004-6361/201016113)
- Buchler, J. R., & Yueh, W. R. 1976, *ApJ*, 210, 440, doi: [10.1086/154847](https://doi.org/10.1086/154847)

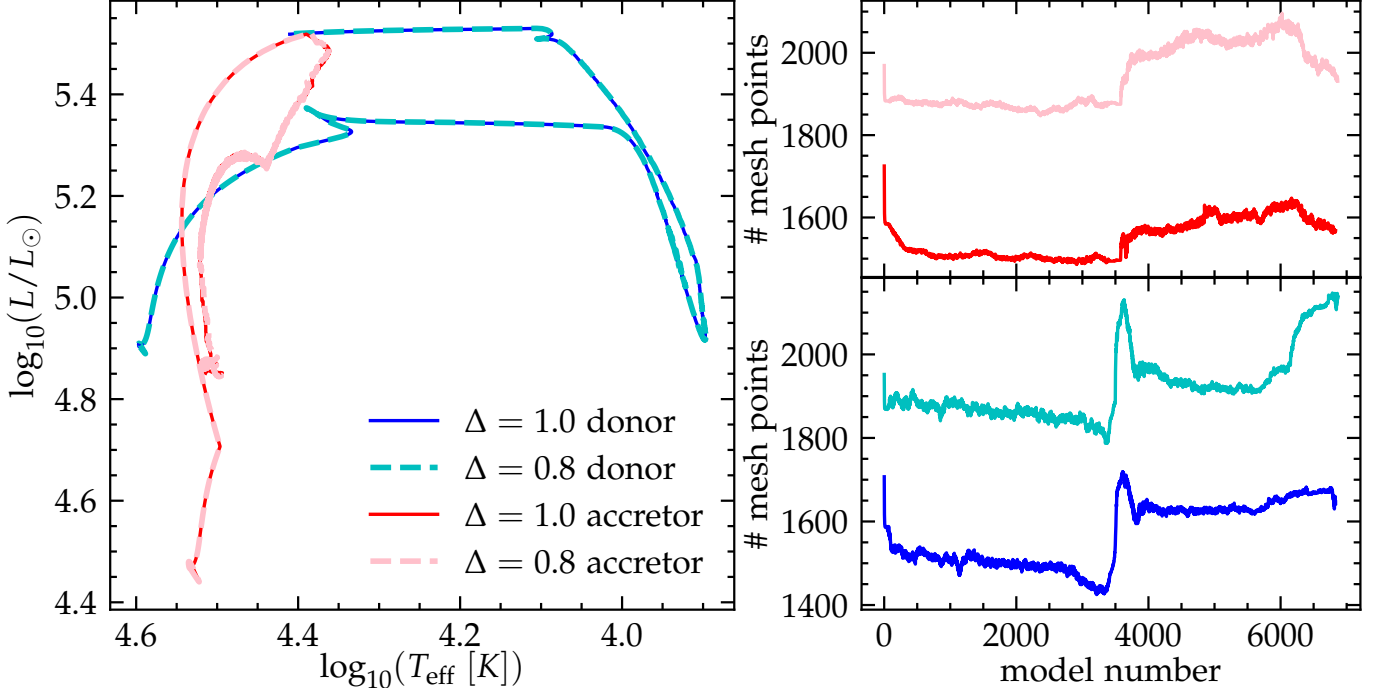


**Figure 8.** Left: HR diagram comparison for our fiducial binary model varying the number of mesh points. We only show the evolution until our definition of RLOF detachment. Right: number of mesh points as a function of timestep number. In both panels, the blue/cyan tracks show the donor stars, the red/pink tracks show the accretor. Thicker dashed lines correspond to the models at higher resolution (i.e., lower  $\Delta$  which indicates the value of `mesh_delta_coeff`).

- Callister, T. A., Farr, W. M., & Renzo, M. 2020, arXiv e-prints, arXiv:2011.09570.  
<https://arxiv.org/abs/2011.09570>
- Cantiello, M., Lecoanet, D., Jermyn, A. S., & Grassitelli, L. 2021, arXiv e-prints, arXiv:2102.05670.  
<https://arxiv.org/abs/2102.05670>
- Cantiello, M., Yoon, S., Langer, N., & Livio, M. 2007, *A&A*, 465, L29
- Cassisi, S., Potekhin, A. Y., Pietrinferni, A., Catelan, M., & Salaris, M. 2007, *ApJ*, 661, 1094, doi: [10.1086/516819](https://doi.org/10.1086/516819)
- Chen, X., & Han, Z. 2009, *MNRAS*, 395, 1822, doi: [10.1111/j.1365-2966.2009.14669.x](https://doi.org/10.1111/j.1365-2966.2009.14669.x)
- . 2010, *Ap&SS*, 329, 277, doi: [10.1007/s10509-010-0368-0](https://doi.org/10.1007/s10509-010-0368-0)
- Chugunov, A. I., Dewitt, H. E., & Yakovlev, D. G. 2007, *PhRvD*, 76, 025028, doi: [10.1103/PhysRevD.76.025028](https://doi.org/10.1103/PhysRevD.76.025028)
- Claret, A., & Torres, G. 2017, *ApJ*, 849, 18, doi: [10.3847/1538-4357/aa8770](https://doi.org/10.3847/1538-4357/aa8770)
- Crowther, P. A. 2007, *ARA&A*, 45, 177, doi: [10.1146/annurev.astro.45.051806.110615](https://doi.org/10.1146/annurev.astro.45.051806.110615)
- Cyburt, R. H., Amthor, A. M., Ferguson, R., et al. 2010, *ApJS*, 189, 240, doi: [10.1088/0067-0049/189/1/240](https://doi.org/10.1088/0067-0049/189/1/240)
- De Donder, E., Vanbeveren, D., & van Bever, J. 1997, *A&A*, 318, 812
- de Jager, C., Nieuwenhuijzen, H., & van der Hucht, K. A. 1988, *A&AS*, 72, 259
- de Mink, S. E., Langer, N., & Izzard, R. G. 2011, *Bulletin de la Societe Royale des Sciences de Liege*, 80, 543.  
<https://arxiv.org/abs/1010.2200>
- de Mink, S. E., Langer, N., Izzard, R. G., Sana, H., & de Koter, A. 2013, *ApJ*, 764, 166, doi: [10.1088/0004-637X/764/2/166](https://doi.org/10.1088/0004-637X/764/2/166)
- Dorigo Jones, J., Oey, M. S., Paggeot, K., Castro, N., & Moe, M. 2020, *ApJ*, 903, 43, doi: [10.3847/1538-4357/abbc6b](https://doi.org/10.3847/1538-4357/abbc6b)
- Ekström, S., Georgy, C., Eggenberger, P., et al. 2012, *A&A*, 537, A146, doi: [10.1051/0004-6361/201117751](https://doi.org/10.1051/0004-6361/201117751)
- Eldridge, J. J., Langer, N., & Tout, C. A. 2011, *MNRAS*, 414, 3501, doi: [10.1111/j.1365-2966.2011.18650.x](https://doi.org/10.1111/j.1365-2966.2011.18650.x)
- Eldridge, J. J., & Stanway, E. R. 2012, *MNRAS*, 419, 479, doi: [10.1111/j.1365-2966.2011.19713.x](https://doi.org/10.1111/j.1365-2966.2011.19713.x)
- Evans, F. A., Renzo, M., & Rossi, E. M. 2020, arXiv e-prints, arXiv:2006.00849.  
<https://arxiv.org/abs/2006.00849>
- Farmer, R. 2018, *rjfarmer/mesaplot*, doi: [10.5281/zenodo.1441329](https://doi.org/10.5281/zenodo.1441329)
- Ferguson, J. W., Alexander, D. R., Allard, F., et al. 2005, *ApJ*, 623, 585, doi: [10.1086/428642](https://doi.org/10.1086/428642)
- Fuller, G. M., Fowler, W. A., & Newman, M. J. 1985, *ApJ*, 293, 1, doi: [10.1086/163208](https://doi.org/10.1086/163208)

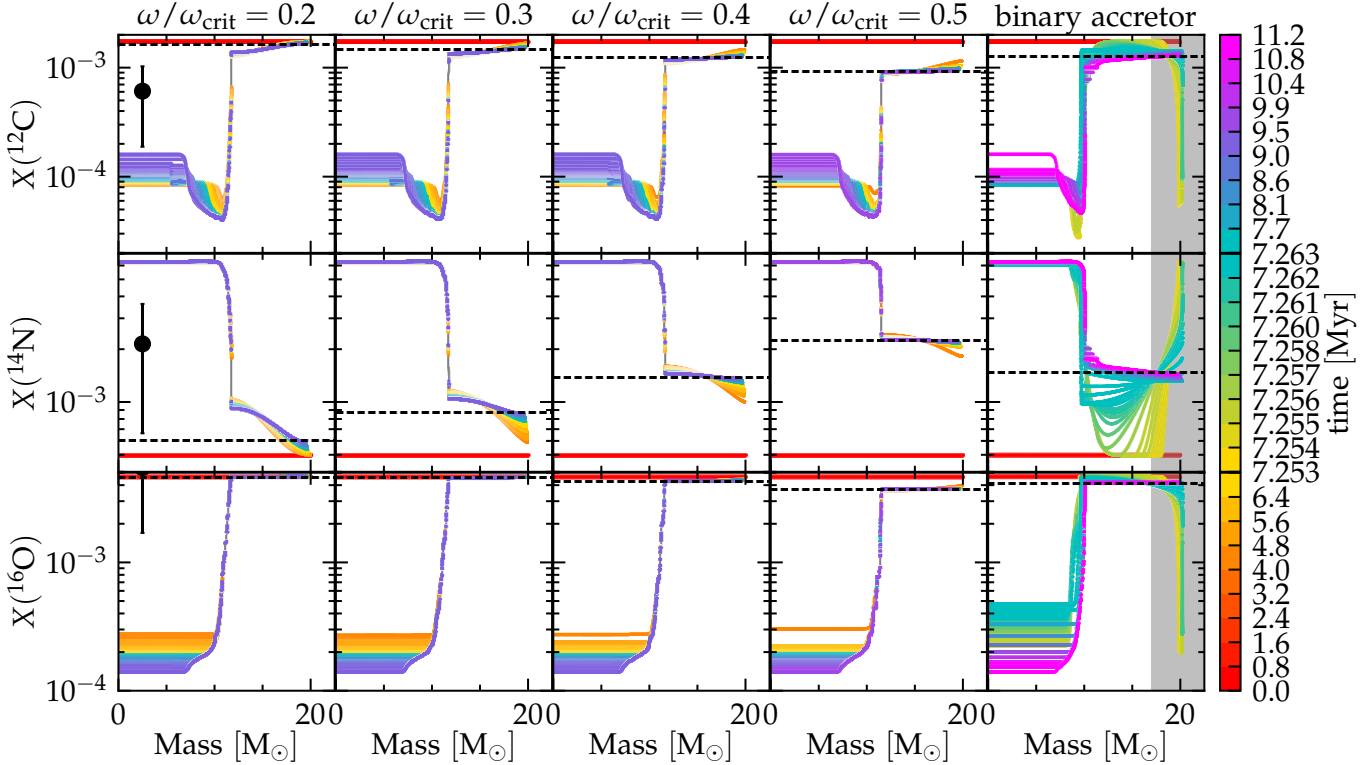


**Figure 9.** Same as Fig. 4, but for  $^{12}\text{C}$  (top panel), and  $^{16}\text{O}$  (bottom panel). The first four panels show single rotating stars of initially  $20 M_{\odot}$ , the rightmost panel shows the accretor in our fiducial binary. The middle panel is exactly the same as Fig. 4. Thick red dotted lines mark the initial mass fractions, thin red dashed lines the TAMS surface mass fraction, the solid red lines and the semi-transparent red bands correspond to the values inferred by VH05 using the surface H mass fraction from our model. The tracks go from dark (roughly corresponding to ZAMS) to light colors, with the lightest color corresponds to TAMS.

Fuller, J., Piro, A. L., & Jermyn, A. S. 2019, MNRAS, 485, 3661, doi: [10.1093/mnras/stz514](https://doi.org/10.1093/mnras/stz514)

Gilkis, A., Vink, J. S., Eldridge, J. J., & Tout, C. A. 2019, MNRAS, 486, 4451, doi: [10.1093/mnras/stz1134](https://doi.org/10.1093/mnras/stz1134)

Gordon, K. D., Gies, D. R., Schaefer, G. H., et al. 2018, ApJ, 869, 37, doi: [10.3847/1538-4357/aaec04](https://doi.org/10.3847/1538-4357/aaec04)

Götberg, Y., de Mink, S. E., & Groh, J. H. 2017, <https://arxiv.org/abs/1701.07439>

Götberg, Y., de Mink, S. E., Groh, J. H., et al. 2018, A&A, 615, A78, doi: [10.1051/0004-6361/201732274](https://doi.org/10.1051/0004-6361/201732274)

Grasha, K., Roy, A., Sutherland, R. S., & Kewley, L. J. 2021, ApJ, 908, 241, doi: [10.3847/1538-4357/abdf6bf](https://doi.org/10.3847/1538-4357/abdf6bf)

Grevesse, N., & Sauval, A. J. 1998, SSRv, 85, 161, doi: [10.1023/A:1005161325181](https://doi.org/10.1023/A:1005161325181)

Heger, A., Langer, N., & Woosley, S. E. 2000, ApJ, 528, 368

Hellings, P. 1983, Ap&SS, 96, 37, doi: [10.1007/BF00661941](https://doi.org/10.1007/BF00661941)  
—. 1984, Ap&SS, 104, 83, doi: [10.1007/BF00653994](https://doi.org/10.1007/BF00653994)

Herrero, A., Kudritzki, R. P., Vilchez, J. M., et al. 1992, A&A, 261, 209

Herwig, F. 2000, A&A, 360, 952

Hirai, R., Podsiadlowski, P., & Yamada, S. 2018, <https://arxiv.org/abs/1803.10808>

Hoogerwerf, R., de Bruijne, J. H. J., & de Zeeuw, P. T. 2000, ApJL, 544, L133, doi: [10.1086/317315](https://doi.org/10.1086/317315)

—. 2001, A&A, 365, 49, doi: [10.1051/0004-6361:20000014](https://doi.org/10.1051/0004-6361:20000014)

Hunter, J. D. 2007, Computing In Science &amp; Engineering, 9, 90

Iglesias, C. A., & Rogers, F. J. 1993, ApJ, 412, 752, doi: [10.1086/172958](https://doi.org/10.1086/172958)

—. 1996, ApJ, 464, 943, doi: [10.1086/177381](https://doi.org/10.1086/177381)

Itoh, N., Hayashi, H., Nishikawa, A., & Kohyama, Y. 1996, ApJS, 102, 411, doi: [10.1086/192264](https://doi.org/10.1086/192264)

Kalogera, V. 1996, ApJ, 471, 352, doi: [10.1086/177974](https://doi.org/10.1086/177974)

Kippenhahn, R., Ruschenplatt, G., & Thomas, H.-C. 1980, A&A, 91, 175

Kippenhahn, R., & Weigert, A. 1967, ZA, 65, 251

Klencki, J., Nelemans, G., Istrate, A. G., & Chruslinska, M. 2021, A&A, 645, A54, doi: [10.1051/0004-6361/202038707](https://doi.org/10.1051/0004-6361/202038707)

Klencki, J., Nelemans, G., Istrate, A. G., & Pols, O. 2020, A&A, 638, A55, doi: [10.1051/0004-6361/202037694](https://doi.org/10.1051/0004-6361/202037694)

Kolb, U., & Ritter, H. 1990, A&A, 236, 385

Lagae, C., Driessen, F. A., Hennicker, L., Kee, N. D., &

Sundqvist, J. O. 2021, arXiv e-prints, arXiv:2103.15904.

<https://arxiv.org/abs/2103.15904>

- Langanke, K., & Martínez-Pinedo, G. 2000, Nuclear Physics A, 673, 481, doi: [10.1016/S0375-9474\(00\)00131-7](https://doi.org/10.1016/S0375-9474(00)00131-7)
- Langer, N. 1998, A&A, 329, 551
- Langer, N., Fricke, K. J., & Sugimoto, D. 1983, A&A, 126, 207
- Laplace, E., Götberg, Y., de Mink, S. E., Justham, S., & Farmer, R. 2020, A&A, 637, A6, doi: [10.1051/0004-6361/201937300](https://doi.org/10.1051/0004-6361/201937300)
- Laplace, E., Justham, S., Renzo, M., et al. 2021, arXiv e-prints, arXiv:2102.05036. <https://arxiv.org/abs/2102.05036>
- Law-Smith, J. A. P., Everson, R. W., Ramirez-Ruiz, E., et al. 2020, arXiv e-prints, arXiv:2011.06630. <https://arxiv.org/abs/2011.06630>
- Ledoux, P. 1947, ApJ, 105, 305, doi: [10.1086/144905](https://doi.org/10.1086/144905)
- Lodders, K. 2019, arXiv e-prints, arXiv:1912.00844. <https://arxiv.org/abs/1912.00844>
- Lubow, S. H., & Shu, F. H. 1975, ApJ, 198, 383, doi: [10.1086/153614](https://doi.org/10.1086/153614)
- Lucy, L. B. 2012, A&A, 544, A120, doi: [10.1051/0004-6361/201118753](https://doi.org/10.1051/0004-6361/201118753)
- Maeder, A., & Meynet, G. 2000, ARA&A, 38, 143, doi: [10.1146/annurev.astro.38.1.143](https://doi.org/10.1146/annurev.astro.38.1.143)
- Marcolino, W. L. F., Bouret, J. C., Martins, F., et al. 2009, A&A, 498, 837, doi: [10.1051/0004-6361/200811289](https://doi.org/10.1051/0004-6361/200811289)
- Mason, B. D., Hartkopf, W. I., Gies, D. R., Henry, T. J., & Helsel, J. W. 2009, AJ, 137, 3358, doi: [10.1088/0004-6256/137/2/3358](https://doi.org/10.1088/0004-6256/137/2/3358)
- Meynet, G., & Maeder, A. 2000, A&A, 361, 101 —. 2003, A&A, 404, 975, doi: [10.1051/0004-6361:20030512](https://doi.org/10.1051/0004-6361:20030512)
- Moe, M., & Di Stefano, R. 2017, ApJS, 230, 15, doi: [10.3847/1538-4365/aa6fb6](https://doi.org/10.3847/1538-4365/aa6fb6)
- Morton, D. C. 1960, ApJ, 132, 146, doi: [10.1086/146908](https://doi.org/10.1086/146908)
- Murphy, S. J., Joyce, M., Bedding, T. R., White, T. R., & Kama, M. 2021, MNRAS, 502, 1633, doi: [10.1093/mnras/stab144](https://doi.org/10.1093/mnras/stab144)
- Neo, S., Miyaji, S., Nomoto, K., & Sugimoto, D. 1977, PASJ, 29, 249
- Neugent, K. F., Massey, P., Hillier, D. J., & Morrell, N. 2017, ApJ, 841, 20, doi: [10.3847/1538-4357/aa6e51](https://doi.org/10.3847/1538-4357/aa6e51)
- Neuhäuser, R., Gießler, F., & Hambaryan, V. V. 2020, MNRAS, 498, 899, doi: [10.1093/mnras/stz2629](https://doi.org/10.1093/mnras/stz2629)
- Nugis, T., & Lamers, H. J. G. L. M. 2000, A&A, 360, 227
- Oda, T., Hino, M., Muto, K., Takahara, M., & Sato, K. 1994, Atomic Data and Nuclear Data Tables, 56, 231, doi: [10.1006/adnd.1994.1007](https://doi.org/10.1006/adnd.1994.1007)
- Packet, W. 1981, A&A, 102, 17
- Paczynski, B. 1976, in IAU Symposium, Vol. 73, Structure and Evolution of Close Binary Systems, ed. P. Eggleton, S. Mitton, & J. Whelan, 75
- Paczynski, B. 1991, ApJ, 370, 597, doi: [10.1086/169846](https://doi.org/10.1086/169846)
- Paxton, B., Bildsten, L., Dotter, A., et al. 2011, ApJS, 192, 3, doi: [10.1088/0067-0049/192/1/3](https://doi.org/10.1088/0067-0049/192/1/3)
- Paxton, B., Cantiello, M., Arras, P., et al. 2013, ApJS, 208, 4, doi: [10.1088/0067-0049/208/1/4](https://doi.org/10.1088/0067-0049/208/1/4)
- Paxton, B., Marchant, P., Schwab, J., et al. 2015, ApJS, 220, 15, doi: [10.1088/0067-0049/220/1/15](https://doi.org/10.1088/0067-0049/220/1/15)
- Paxton, B., Schwab, J., Bauer, E. B., et al. 2018, ApJS, 234, 34, doi: [10.3847/1538-4365/aaa5a8](https://doi.org/10.3847/1538-4365/aaa5a8)
- Paxton, B., Smolec, R., Gautschy, A., et al. 2019. <https://arxiv.org/abs/1903.01426>
- Pecaut, M. J., & Mamajek, E. E. 2016, MNRAS, 461, 794, doi: [10.1093/mnras/stw1300](https://doi.org/10.1093/mnras/stw1300)
- Pérez, F., & Granger, B. E. 2007, Computing in Science & Engineering, 9, 21
- Perna, R., Duffell, P., Cantiello, M., & MacFadyen, A. I. 2014, ApJ, 781, 119, doi: [10.1088/0004-637X/781/2/119](https://doi.org/10.1088/0004-637X/781/2/119)
- Podsiadlowski, P. 2003, arXiv e-prints, astro. <https://arxiv.org/abs/astro-ph/0303660>
- Pols, O. R., Cote, J., Waters, L. B. F. M., & Heise, J. 1991, A&A, 241, 419
- Pols, O. R., & Marinus, M. 1994, A&A, 288, 475
- Pols, O. R., Tout, C. A., Eggleton, P. P., & Han, Z. 1995, MNRAS, 274, 964, doi: [10.1093/mnras/274.3.964](https://doi.org/10.1093/mnras/274.3.964)
- Popham, R., & Narayan, R. 1991, ApJ, 370, 604, doi: [10.1086/169847](https://doi.org/10.1086/169847)
- Potekhin, A. Y., & Chabrier, G. 2010, Contributions to Plasma Physics, 50, 82, doi: [10.1002/ctpp.201010017](https://doi.org/10.1002/ctpp.201010017)
- Przybilla, N., Nieva, M. F., Heber, U., & Butler, K. 2008, The Astrophysical Journal, 684, L103, doi: [10.1086/592245](https://doi.org/10.1086/592245)
- Qin, Y., Fragos, T., Meynet, G., et al. 2018, A&A, 616, A28, doi: [10.1051/0004-6361/201832839](https://doi.org/10.1051/0004-6361/201832839)
- Rain, M. J., Ahumada, J., & Carraro, G. 2021, arXiv e-prints, arXiv:2103.06004. <https://arxiv.org/abs/2103.06004>
- Ramírez-Agudelo, O. H., Simón-Díaz, S., Sana, H., et al. 2013, A&A, 560, A29, doi: [10.1051/0004-6361/201321986](https://doi.org/10.1051/0004-6361/201321986)
- Ramírez-Agudelo, O. H., Sana, H., de Mink, S. E., et al. 2015, A&A, 580, A92, doi: [10.1051/0004-6361/201425424](https://doi.org/10.1051/0004-6361/201425424)
- Renzo, M., Farmer, R. J., Justham, S., et al. 2020, arXiv e-prints, arXiv:2002.08200. <https://arxiv.org/abs/2002.08200>
- Renzo, M., Ott, C. D., Shore, S. N., & de Mink, S. E. 2017, A&A, 603, A118, doi: [10.1051/0004-6361/201730698](https://doi.org/10.1051/0004-6361/201730698)
- Renzo, M., Zapartas, E., de Mink, S. E., et al. 2019, A&A, 624, A66, doi: [10.1051/0004-6361/201833297](https://doi.org/10.1051/0004-6361/201833297)
- Rogers, F. J., & Nayfonov, A. 2002, ApJ, 576, 1064, doi: [10.1086/341894](https://doi.org/10.1086/341894)

- Sana, H., de Mink, S. E., de Koter, A., et al. 2012, Science, 337, 444, doi: [10.1126/science.1223344](https://doi.org/10.1126/science.1223344)
- Saumon, D., Chabrier, G., & van Horn, H. M. 1995, ApJS, 99, 713, doi: [10.1086/192204](https://doi.org/10.1086/192204)
- Schneider, F. R. N., Izzard, R. G., Langer, N., & de Mink, S. E. 2015, ApJ, 805, 20, doi: [10.1088/0004-637X/805/1/20](https://doi.org/10.1088/0004-637X/805/1/20)
- Schneider, F. R. N., Podsiadlowski, P., Langer, N., Castro, N., & Fossati, L. 2016, MNRAS, 457, 2355, doi: [10.1093/mnras/stw148](https://doi.org/10.1093/mnras/stw148)
- Schneider, F. R. N., Podsiadlowski, P., & Müller, B. 2021, A&A, 645, A5, doi: [10.1051/0004-6361/202039219](https://doi.org/10.1051/0004-6361/202039219)
- Schootemeijer, A., Langer, N., Grin, N. J., & Wang, C. 2019, A&A, 625, A132, doi: [10.1051/0004-6361/201935046](https://doi.org/10.1051/0004-6361/201935046)
- Sota, A., Maíz Apellániz, J., Morrell, N. I., et al. 2014, ApJS, 211, 10, doi: [10.1088/0067-0049/211/1/10](https://doi.org/10.1088/0067-0049/211/1/10)
- Spruit, H. C. 2002, A&A, 381, 923, doi: [10.1051/0004-6361:20011465](https://doi.org/10.1051/0004-6361:20011465)
- Sravan, N., Marchant, P., & Kalogera, V. 2019, ApJ, 885, 130, doi: [10.3847/1538-4357/ab4ad7](https://doi.org/10.3847/1538-4357/ab4ad7)
- Suda, T., Saitoh, T. R., Moritani, Y., Matsuno, T., & Shigeyama, T. 2021, arXiv e-prints, arXiv:2103.13627. <https://arxiv.org/abs/2103.13627>
- Sweet, P. A. 1950, MNRAS, 110, 548, doi: [10.1093/mnras/110.6.548](https://doi.org/10.1093/mnras/110.6.548)
- Tauris, T. M. 2015, MNRAS, 448, L6, doi: [10.1093/mnrasl/slu189](https://doi.org/10.1093/mnrasl/slu189)
- Tauris, T. M., & Takens, R. J. 1998, A&A, 330, 1047
- Tauris, T. M., Kramer, M., Freire, P. C. C., et al. 2017, ApJ, 846, 170, doi: [10.3847/1538-4357/aa7e89](https://doi.org/10.3847/1538-4357/aa7e89)
- Tetzlaff, N., Neuhäuser, R., Hohle, M. M., & Maciejewski, G. 2010, MNRAS, 402, 2369, doi: [10.1111/j.1365-2966.2009.16093.x](https://doi.org/10.1111/j.1365-2966.2009.16093.x)
- Timmes, F. X., & Swesty, F. D. 2000, ApJS, 126, 501, doi: [10.1086/313304](https://doi.org/10.1086/313304)
- Townsend, R. 2018, MESA SDK for Linux: 20180822, doi: [10.5281/zenodo.2603170](https://doi.org/10.5281/zenodo.2603170)
- Ulrich, R. K., & Burger, H. L. 1976, ApJ, 206, 509, doi: [10.1086/154406](https://doi.org/10.1086/154406)
- van der Walt, S., Colbert, S. C., & Varoquaux, G. 2011, Computing in Science Engineering, 13, 22, doi: [10.1109/MCSE.2011.37](https://doi.org/10.1109/MCSE.2011.37)
- van Rensbergen, W., de Greve, J. P., Mennekens, N., Jansen, K., & de Loore, C. 2011, A&A, 528, A16, doi: [10.1051/0004-6361/201015596](https://doi.org/10.1051/0004-6361/201015596)
- van Rensbergen, W., De Loore, C., & Jansen, K. 2006, A&A, 446, 1071, doi: [10.1051/0004-6361:20053543](https://doi.org/10.1051/0004-6361:20053543)
- van Rensbergen, W., Vanbeveren, D., & De Loore, C. 1996, A&A, 305, 825
- Vartanyan, D., Laplace, E., Renzo, M., et al. 2021, arXiv e-prints, arXiv:2104.03317. <https://arxiv.org/abs/2104.03317>
- Villamariz, M. R., & Herrero, A. 2005, A&A, 442, 263, doi: [10.1051/0004-6361:20052848](https://doi.org/10.1051/0004-6361:20052848)
- Vinciguerra, S., Neijssel, C. J., Vigna-Gómez, A., et al. 2020, MNRAS, 498, 4705, doi: [10.1093/mnras/staa2177](https://doi.org/10.1093/mnras/staa2177)
- Vink, J. S. 2017, A&A, 607, L8, doi: [10.1051/0004-6361/201731902](https://doi.org/10.1051/0004-6361/201731902)
- Vink, J. S., Davies, B., Harries, T. J., Oudmaijer, R. D., & Walborn, N. R. 2009, A&A, 505, 743, doi: [10.1051/0004-6361/200912610](https://doi.org/10.1051/0004-6361/200912610)
- Vink, J. S., de Koter, A., & Lamers, H. J. G. L. M. 2000, A&A, 362, 295
- . 2001, A&A, 369, 574, doi: [10.1051/0004-6361:20010127](https://doi.org/10.1051/0004-6361:20010127)
- Walker, G. A. H., Yang, S., & Fahlman, G. G. 1979, ApJ, 233, 199, doi: [10.1086/157381](https://doi.org/10.1086/157381)
- Walker, G. A. H., Kuschnig, R., Matthews, J. M., et al. 2005, ApJL, 623, L145, doi: [10.1086/430254](https://doi.org/10.1086/430254)
- Wang, C., Langer, N., Schootemeijer, A., et al. 2020, ApJL, 888, L12, doi: [10.3847/2041-8213/ab6171](https://doi.org/10.3847/2041-8213/ab6171)
- Wang, L., Gies, D. R., Peters, G. J., et al. 2021, arXiv e-prints, arXiv:2103.13642. <https://arxiv.org/abs/2103.13642>
- Wei, D., Wang, B., Chen, H., et al. 2021, arXiv e-prints, arXiv:2105.00291. <https://arxiv.org/abs/2105.00291>
- Wheeler, J. C., Lecar, M., & McKee, C. F. 1975, ApJ, 200, 145, doi: [10.1086/153771](https://doi.org/10.1086/153771)
- Yoon, S.-C., Dessart, L., & Clocchiatti, A. 2017, ApJ, 840, 10, doi: [10.3847/1538-4357/aa6afe](https://doi.org/10.3847/1538-4357/aa6afe)
- Yoon, S.-C., Langer, N., & Norman, C. 2006, A&A, 460, 199, doi: [10.1051/0004-6361:20065912](https://doi.org/10.1051/0004-6361:20065912)
- Zahn, J. P. 1992, A&A, 265, 115
- Zaldarriaga, M., Kushnir, D., & Kollmeier, J. A. 2018, MNRAS, 473, 4174, doi: [10.1093/mnras/stx2577](https://doi.org/10.1093/mnras/stx2577)
- Zapartas, E., de Mink, S. E., Justham, S., et al. 2021, A&A, 645, A6, doi: [10.1051/0004-6361/202037744](https://doi.org/10.1051/0004-6361/202037744)
- . 2019. <https://arxiv.org/abs/1907.06687>
- Zehe, T., Mugrauer, M., Neuhäuser, R., et al. 2018, Astronomische Nachrichten, 339, 46, doi: [10.1002/asna.201713383](https://doi.org/10.1002/asna.201713383)
- Zhao, X., & Fuller, J. 2020, MNRAS, 495, 249, doi: [10.1093/mnras/staa1097](https://doi.org/10.1093/mnras/staa1097)